AIAA Propulsion and Energy 2017, July 10–12, Atlanta, GA

A Critical Review of Thrust Models for Applied-Field Magnetoplasmadynamic Thrusters

William J. Coogan[*] and Edgar Y. Choueiri[†]

Princeton University, Princeton, NJ, 08544, USA

A critical review of published thrust models for applied-field magnetoplasmadynamic thrusters is presented, along with a new model addressing shortcomings related to electrode and magnet geometry. While numerous theoretical thrust models have been presented in the literature, there has not been a comprehensive comparison to determine which best predicts thruster behavior across a large parameter space. In order to make this determination, all thrust data available in the literature were collected into a single database and tested against each model. Unlike previous comparisons between prediction and measurement, only the regime in which the applied-field thrust component dominates is examined, allowing for a direct comparison without invoking models of self-field and gasdynamic components of thrust. The degree to which each model deviates from measurement is determined for each controllable parameter. It is found that the largest deviations are due to incorrect representation of the effects of electrode and solenoid geometries. In light of this comparative study, an improved empirical model is derived as a function of nondimensional parameters representing these geometric variables. The improved agreement is attributed to the effects of magnetic field topology near the anode, which sets the effective anode radius that controls the magnitude of the Lorentz force for certain electrode geometries.

Nomenclature

B_A	Applied magnetic field, T
c_s	Sound speed, m/s
F	Force density, N/m^3
j	Current density, A/m^2
J	Current, A
k	Scaling constant
k_B	Boltzmann constant, J/K
l	Axial length, m
$\dot{m}$	Mass flow rate, kg/s
M	Atomic mass, u
n	Density, m^{-3}
N_A	Avogadro's number
p_b	Background pressure, mTorr
r	Radius, m
$\bar{r}$	Ratio of anode radius to cathode radius
r^*	Characteristic length scale, m
$\hat{r}$	Percentage distance between inner and outer surfaces
$\hat{r}^*$	Percentage distance at which $\hat{s}$ is minimized
r_B	Average solenoid radius, m
r_Bi	Inner solenoid radius, m
r_Bo	Outer solenoid radius, m
$\hat{s}$	Relative standard deviation
T	Thrust, N
$\bar{T}$	Dimensionless thrust parameter
$\hat{\bar{T}}$	Normalized thrust parameter
$\mathcal{T}$	Temperature, K
u_ex	Exhaust velocity, m/s
V	Voltage, V
$\bar{Y}$	Ionization factor
z	Distance from solenoid along thrust axis
Z	Charge number
α	Degree of ionization
β	Ratio of gasdynamic to magnetic pressure
γ	Adiabatic index
ϵ_i	Ionization energy, eV
ζ	Detachment parameter, s^6/m^9
κ	Scaling constant

---

[*] Graduate Student, MAE Dept., Princeton University, AIAA Student Member.

[†] Chief Scientist, EPPDyL, Professor, Applied Physics Group, MAE Dept., Princeton University, AIAA Fellow.

θ_{div}	Plume divergence angle from thrust axis at detachment point
μ_0	Permeability of free space, N/A^2
ν_{ei}	Electron-ion collision frequency, s^{-1}
ξ	Additive constant
Φ	Magnetic flux, T $\cdot$ m^2
$\bar{\Phi}$	Contour of anode to magnetic field
ω	Plasma rotation rate, s^{-1}

Subscripts

a	Anode
a0	Anode throat or backplate
ae	Anode exit plane
AF	Applied-field
c	Cathode
e	Electron
eff	Effective value
GD	Gasdynamic
H	Hall
i	Ion
SF	Self-field
SW	Swirl
z	Direction of thrust axis
$-\Phi$	With respect to surface of constant magnetic flux
-0	With respect to anode throat

I. Introduction

Since the 1960s, the applied-field magnetoplasmadynamic thruster (AF-MPDT) has been presented as a high-thrust density alternative to other forms of electric propulsion.[1] While the power requirements for this thruster have made it an infeasible option for space exploration up until the present, AF-MPDT operation may become possible in the near- to mid-term due to the projection for as much as 200 kW of solar power for spacecraft.[2,3] However, questions remain as to how to optimize the performance of this thruster for a given mission's requirements. Of primary concern here is a model with which to determine the achievable thrust for a given set of operating and geometric parameters.

The thrust of an AF-MPDT is typically assumed to be the sum of the applied-field, self-field, and gasdynamic thrust components.[4–9] While we overview each of these components, our focus is on analytical models of the applied-field thrust since the mechanisms behind self-field thrust are simpler and far better understood,[10,11] and because gasdynamic thrust is negligible under nominal operating conditions.[9,12,13] There are many applied-field thrust models,[1,5,7,9,12–16] but what is lacking is a comparison of each of them to measurement across a large parameter space.

With the goal of making such a comparison, we have assembled an exhaustive database of published thrust measurements. In order to compare a model of the applied-field component of the thrust to a measurement of the total thrust, we restrict our comparison to regimes where the applied-field component dominates. We determine the ability of each model to predict the magnitude of the thrust, as well as the thrust dependence on controllable parameters. These parameters include both operating parameters, such as current, applied-field strength, propellant, and mass flow rate, and geometric ones, such as electrode and solenoid length scales.

In light of that comparison, we formulate an empirical model that aims to better predict measurement. We use nondimensional analysis to account for dependencies not captured by previous models and seek insight into the physics underlying the scaling of thrust with our nondimensional parameters.

In Sec. II, we give an overview of the different thrust models for AF-MPDTs and the assumptions made in each. In Sec. III, we describe the performance data we collected from a multitude of sources in the literature and provide a summary of each thruster in this survey. Section IV describes facility effects on thrust and the criteria we set to determine data validity. We explain the model-experiment comparison methodology in Sec. V followed by the results of this comparison for existing models in Sec. VI. In view of these results, and the shortcomings of the existing models, we empirically derive a new model using Π products and give the results of this model in Sec. VII, along with an explanation of the underlying physics.

II. Thrust Models

The thrust generated by an AF-MPDT is generally assumed to be the sum of three different components: the applied-field (AF), the self-field (SF), and the gasdynamic (GD). Since the focus of this paper is on the applied-field thrust, we review all published models of that component. This is followed by a brief description of self-field and gasdynamic thrust as they are essential to some of these applied-field thrust models.

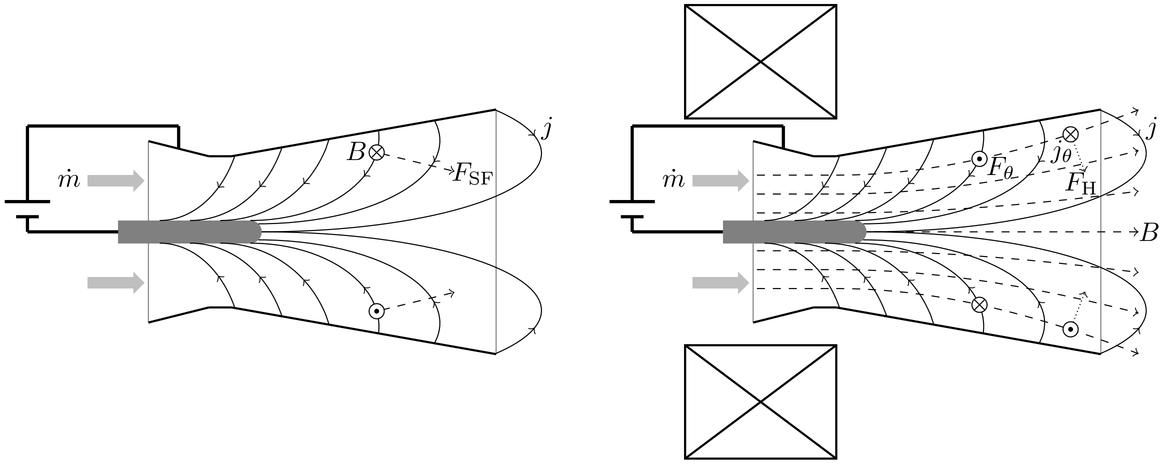

(a) Self-field Lorentz force **(b) Applied-field Lorentz force**

Figure 1: Lorentz forces resulting from a self-induced magnetic field (a) and from an external magnetic field (b) shown in schematic cross-sections of MPDTs. The external magnetic field adds azimuthal and Hall-effect forces (F_θ and F_{H} respectively) to the self-field force (F_{SF}).

A. Applied-Field Thrust Component

As shown in Fig. 1 (b), the mostly axial external magnetic field crossed with the radial component of the current swirls the plasma. This bulk swirling motion is converted into axial thrust as the rotating body expands through the diverging applied field and then detaches from the field lines. The swirling motion also results in an azimuthal Hall current due to the collisional nature of AF-MPDTs, which preferentially allows electrons to travel azimuthally. This Hall current crossed with the radial component of the diverging applied magnetic field generates additional thrust. It is these two thrust mechanisms, resulting from the applied field, that are the focus for this paper, and which are the dominant thrust producing mechanisms in most AF-MPDTs.

Many models of the applied-field thrust are similar in nature, predicting that $T_{\mathrm{AF}} \propto JB_{\mathrm{A}}r$, where T_{AF} is the applied-field thrust component, J is the current, B_{A} is the applied field strength, and r is a characteristic electrode length scale. We categorize these as "$JB_{\mathrm{A}}r$" models. In addition, there are three models which assume a more complicated relationship between thrust and the parameters upon which it depends. These we categorize as "non-$JB_{\mathrm{A}}r$" models.

$JB_{\mathrm{A}}r$ MODELS

1. Fradkin et al.:[14]

Fradkin et al. assume a strictly axial magnetic field in the thruster volume, derive the torque resulting from the radial current and the applied field, and then assume this torque acts to rotate the plasma inside the thruster as a rigid rotor. Assuming all of the resulting azimuthal kinetic energy is converted into axial kinetic energy, they find that

$$T_{\mathrm{Fradkin}} = JB_{\mathrm{A}}\frac{r_{\mathrm{a}}^2 - r_{\mathrm{c}}^2}{\sqrt{2(r_{\mathrm{a}}^2 + r_{\mathrm{c}}^2)}}, \tag{1}$$

where T_{Fradkin} is the predicted upper limit for the applied-field component of the thrust, B_{A} is the applied magnetic field strength (assumed to be constant in the thruster volume), r_{c} is the cathode radius, and r_{a} is the anode radius.

Fradkin et al. derive this equation for a particular geometry that may not be relevant to all thrust data used in this survey. A cylindrical rotating body is assumed, with a hollow core accounting for a cathode that extends through the anode volume. Many thrusters have anodes whose radii vary axially and/or cathodes that do not extend into the anode volume. Further, the assumption of a constant, purely axial magnetic field is less valid for smaller solenoid radii unless the anode is completely enclosed by the solenoid. The largest solenoid in the literature is that employed by the Moscow Aviation Institute for the 150 and 200 kW Li thrusters, for which the magnetic field strength decreases by a factor of 2 in the span of the anode length, indicating significant divergence.

2. *Myers:*[15]

Using the Fradkin et al. model as a starting point, Myers derives an expression for the applied-field thrust component empirically based on his experiments with 100 kW class AF-MPDTs using a variety of different electrode geometries. He finds that

$$T_{\mathrm{Myers}} = J B_{\mathrm{A}} \frac{r_{\mathrm{a}}^2}{500 r_{\mathrm{c}} l_{\mathrm{c}}}, \tag{2}$$

where l_{c} is the length of the cathode and the constant 500 has dimensions of m^{-1}. This model predicts an influence of the cathode geometry that is significant, whereas that predicted by Fradkin et al. can be neglected for $r_{\mathrm{a}} \gg r_{\mathrm{c}}$. Myers incorporates his observation that thrust decreases with cathode length in the regime in which he operated, however this makes the equation inapplicable to thrusters with recessed cathodes, for which $l_{\mathrm{c}} \leq 0$.

3. *Albertoni et al.:*[9]

Albertoni et al. apply an empirically-derived nondimensional scaling constant, k, to the Fradkin et al. model to fit the data for a given thruster, so that

$$T_{\mathrm{Albertoni}} = k_{\mathrm{Albertoni}} T_{\mathrm{Fradkin}}. \tag{3}$$

This constant can be determined experimentally for each thruster and is representative of the degree to which the conversion of azimuthal motion to axial motion takes place within the magnetic nozzle. In our application of this model, we set $k = 0.25$, which is reported in Ref. 9 to result in good general agreement between prediction and the measurements against which the model was originally compared.

4. *Tikhonov et al.:*[7, 17]

In contrast to the model presented by Fradkin et al., which assumes a constant magnetic field in the thruster volume, Tikhonov et al. derive an analytical model assuming that the thrust is the result of the Hall current crossing the diverging magnetic field. While they reach an analytic expression, they lump many of the terms together into one coefficient that is determined empirically,[4, 8, 18–20] giving the equation

$$T_{\mathrm{Tikhonov}} = 0.2 J B_{\mathrm{A}} r_{\mathrm{a}}. \tag{4}$$

The empirically derived coefficient is based on a number of parameters related to the electrode and magnet geometry and may therefore vary from one thruster to another. However, since we seek a model than can predict measurement *a priori*, we treat the coefficient as a constant. In the limit where $r_{\mathrm{a}} \gg r_{\mathrm{c}}$, this model and that of Fradkin et al. agree to within a scaling constant. Outside of this limit, we expect the absence of any r_{c} dependence in this model to make r_{c} an important parameter for comparing the predictive power of the two models.

5. *Herdrich et al.:*[5]

The model of Herdrich et al. uses the model of Tikhonov et al. as a starting point, but they model the coefficient as a function of r_{a}, which they obtain from the data using a power law fit, yielding the equation

$$T_{\mathrm{Herdrich}} = 2.924 J B_{\mathrm{A}} r_{\mathrm{a}}^{1.6577}, \tag{5}$$

where the scaling constant has dimensions of m$^{-0.6577}$. While this yields better agreement with the data, it is unclear whether this agreement is due to a more accurate representation of the effects of the anode radius itself, rather than the solenoid radius or cathode radius, that frequently scale with anode radius.

6. Krülle Model:[1]

In his model, Krülle uses resistive magnetohydrodynamics and assumes that the plasma swirls as a rigid rotor, but notes that his measured thrust depends linearly on magnetic field strength, rather than quadratically as is predicted by his model. He attributes this discrepancy to current outflow beyond the anode exit plane. Because he points out this discrepancy, we mention this model for completeness, but do not include it in the statistical analysis that follows.

NON-$JB_\mathrm{A}r$ MODELS

7. Mikellides and Turchi:[16]

Mikellides and Turchi derive a model that is based on results from MACH2, a numerical simulation tool, which they used to simulate a 100 kW class argon thruster. Their model assumes that the Lorentz force rotates the plasma, generating a shear due to the plasma viscosity. The primary acceleration mechanism in this model is the conversion of thermal energy from viscous heating into directed kinetic energy. They obtain

$$T_\mathrm{Mikellides} = \frac{25}{M^{1/4}}\sqrt{\frac{r_\mathrm{c}}{l_\mathrm{c}\bar{Y}}}\,\frac{\bar{r}(\bar{r}+1)\sqrt{\bar{r}-1}\sqrt{\dot{m}JB_\mathrm{A}}}{\sqrt{\bar{r}^{3.8}-1}}, \tag{6}$$

where $\bar{r}$ is the ratio of anode radius to cathode radius, $\dot{m}$ is the mass flow rate, M is the atomic mass (values given Table 5), and $\bar{Y}$ is the ionization factor. This ionization factor is a measure of the ionization states in the plasma, and is defined by

$$\bar{Y} = \sum_i \left(\frac{\alpha_i}{\sum_j \alpha_j^2 Z_i^2 Z_j^2}\right), \tag{7}$$

where α is the degree of ionization and Z is the charge number. While Ref. 16 provides $\bar{Y}$ values for H_2, Li, and Ar, we cannot determine $\bar{Y}$ analytically without knowing the degree of ionization for each state, which Mikellides and Turchi find through their numerical simulation. Since we are using data for a multitude of propellants, including heteronuclear species, and further since thrust depends weakly on $\bar{Y}$ for typical ionization fractions, we let $\bar{Y} = 1$ for all of our calculations. This assumes that the plasma is completely and singly ionized. We therefore expect any disagreement between this model and our implementation of it to be correlated with ionization energy, ϵ_i, of a given propellant, and consequently test the predictions of each model against measurement as a function of ϵ_i in Sec. VI.

This model makes two unique predictions. First, thrust is predicted to have a strong dependence on $\dot{m}$, resulting from the modeled influence of plasma viscosity. Second, Mikellides and Turchi predict $T_\mathrm{AF} \propto \sqrt{JB_\mathrm{A}}$ whereas it has long been assumed and repeatedly verified experimentally to be proportionate to JB_A.[1,15,21–23] Also worth noting is that the inverse dependence on l_c, as with the Myers model, makes this model incompatible with certain thruster geometries.

8. Sasoh and Arakawa:[13]

Sasoh and Arakawa use energy conservation, as well as Ohm's law, to derive the total work done within the anode. Then, they assume that this work is converted into directed kinetic energy, generating thrust. Central to this model is the contribution of azimuthal currents and the resulting Lorentz force from the radial component of the expanding magnetic field. They find the total thrust to be

$$T_\mathrm{Sasoh} = \frac{T_\mathrm{H}+T_\mathrm{SF}}{2} + \sqrt{\left(\frac{T_\mathrm{H}+T_\mathrm{SF}}{2}\right)^2 + T_\mathrm{SW}^2}, \tag{8}$$

where T_H, T_SF, and T_SW are the thrust components due to the Hall effect, the self-field, and the azimuthally accelerated plasma respectively. This expression differs from our previous description of the total thrust as the sum of several components. This is due to its derivation from an energy balance rather than a momentum balance. The result is that T_SF as described here is not necessarily the same as that described by Eq. 10.

The individual expressions Sasoh and Arakawa provide for the thrust components have too many dependencies to express in a concise form appropriate to a review, so we summarize the assumptions we made in our application of this model and direct the reader to Ref. 13 for the explicit expressions.

Our primary difficulty implementing this model as a *predictive* one stems from its dependence on terms for which we require measurement, such as electron temperature or density, or for which no procedure is provided, such as a characteristic length scale. We assume the plasma temperature, $\mathcal{T}_\mathrm{e} = 2$ eV, which is the order of the temperature found in AF-MPDTs,[8, 24, 25] although higher temperatures have also been reported.[26] We find the density by assuming quasi-neutrality of the plasma and a constant mass flux through the anode volume with ions traveling at the sound speed. We assume the characteristic electrode length to be at a distance r^* from the thrust axis such that $(r^* - r_\mathrm{c})/(r_\mathrm{a} - r_\mathrm{c}) = 0.1$, since this is the value used by Sasoh and Arakawa to verify their model using their own data.

The Sasoh and Arakawa model also requires knowledge of the radial and axial components of the magnetic field, which we find using the Biot-Savart law. A more complete record of the equations used for the evaluation of the magnetic field, electron density, and characteristic length is given in Appendix A.

9. Coletti:[12]

While the model of Fradkin et al. predicts the amount of thrust *possible* from the swirling plasma being redirected in a magnetic nozzle, Coletti models the degree to which this redirection occurs by deriving the plasma velocity and trajectory at the point of detachment. Detachment is assumed to occur when the Alfvén velocity is reached.[27]

Coletti's derivation divides the thrust mechanisms into two distinct physical regions: the anode volume, where plasma acceleration is the result of self-field and applied-field forces, and the magnetic nozzle downstream of the anode volume, where conservation of both energy and the magnetic moment redirect the velocity toward the magnetic field lines. He finds the velocity parallel to the magnetic field at the point of detachment, which, along with the angle of the field with respect to the thrust axis, θ_div, determines the total thrust. This angle is found from the divergence of the magnetic field at the point of detachment.[28] He determines the thrust,

$$T_\mathrm{Coletti} = \frac{1}{2}\left(v_{z,\mathrm{ae}} + \sqrt{v_{z,\mathrm{ae}}^2 + \omega^2 r_\mathrm{a}^2 - \omega^8 r_\mathrm{a}^8 \frac{r_\mathrm{B}^3}{\zeta}}\cos\left(\theta_\mathrm{div}\right)\right)\dot{m}, \tag{9}$$

where $v_{z,\mathrm{ae}}$ is the plasma velocity found using the Maecker formula (Eq. 10), r_B is the solenoid radius, ω is the rate of plasma rotation inside the thruster volume, and ζ is a function of the rotational velocity of the plasma and the axial position at detachment. The rate of rotation is found from the radial current crossed with the axial applied magnetic field, with the assumption that the plasma rotates rigidly.

The Coletti model reduces to Eq. 10 when $B_\mathrm{A} \to 0$, however there are instances in which the third term under the square root can result in a predicted thrust less than that predicted by Eq. 10. In these instances, we use the value predicted by Eq. 10 as is prescribed in Ref. 12. Relevant to this model is the recent research by Ahedo and Merino,[29] which shows that the plasma detachment conditions assumed in this model do not apply to propulsive magnetic nozzles. Nonetheless, without an alternative detachment model, we use the Coletti model as it stands for all reported results.

B. Self-Field Thrust Component:

The self-field thrust component is the result of a Lorentz force generated by the interaction between the current through the plasma and a self-induced magnetic field, as is illustrated in Fig. 1 (a). This thrust component is often assumed to be

$$T_\mathrm{SF} = \frac{\mu_0}{4\pi}\left[\ln\left(\frac{r_\mathrm{a}}{r_\mathrm{c}}\right) + \frac{3}{4}\right] J^2, \tag{10}$$

as modeled by Maecker.[10] Maecker did not originally include the constant $3/4$, but Jahn showed how constants on the order of unity can be assumed depending on variations in the cathode geometry,[30] and $3/4$ tends to provide the best agreement with data at high current levels.[31]

The Maecker formula does not fully describe the performance of SF-MPDTs. The discrepancy between prediction and measurement has been well-described in Ref. 11, which shows that at low $J^2/\dot{m}$ values, the thrust measured can be as high as double that predicted by the Maecker formula. This is attributed to a gasdynamic pressure created by the pinching component of the volumetric Lorentz force.

C. Gasdynamic Thrust Component:

The gasdynamic thrust component, T_{GD}, results from the conversion of thermal energy into directed kinetic energy by means of a nozzle. While it is often assumed to be negligible in a high-power regime, at low JB_{A} values or high $\dot{m}$ values the gasdynamic thrust component can be substantial or even dominant. This component is dependent on the mass flow rate, the velocity at the injection site, the gasdynamic pressure inside the nozzle, and the nozzle area over which that pressure is applied. This component is usually described as

$$T_{\mathrm{GD}} = k_{\mathrm{GD}} \dot{m} c_{\mathrm{s}}, \tag{11}$$

where c_{s} is the ion sound speed and k_{GD} is a nondimensional coefficient on the order of unity.[4–9] The magnitude of k_{GD} has been modeled as being dependent on the angle of the gas flow with respect to the thrust axis[6] or as a function of an additional pressure acting over the area of the injection site.[32] Ref. 32 determines $k_{\mathrm{GD}} = 1 + {}^{1}\!/_{\gamma}$ for a 100 kW lithium thruster with mass injection through the cathode. For polyatomic propellants, γ is poorly defined, but the range of this value is small enough not to change the order of the value predicted by Eq. 11.

There are few measurements of ion temperature, T_{i}, in MPDTs, but those that exist[33–35] indicate that operating temperatures are in the range of 2–20 eV.

D. Controllable Parameters

With data spanning a sufficiently varied parameter space, it is possible to determine which of these models correctly predicts thrust scaling as a function of a given controllable parameter. For example, we can determine if $T_{\mathrm{AF}} \propto r_{\mathrm{a}}$ as predicted by Tikhonov et al. or if $T_{\mathrm{AF}} \propto r_{\mathrm{a}}^{1.6577}$ as Herdrich et al. predicted. In Sec. VI we show how each model's prediction-to-measurement ratio varies as a function of each controllable parameter.

In addition to dimensional parameters such as J or B_{A}, we investigate several nondimensional parameters, most of which are geometric in nature, such as the anode to cathode radius, $r_{\mathrm{a}}/r_{\mathrm{c}}$. One nondimensional parameter that has not previously been explored with respect to AF-MPDTs describes the degree to which the anode inner surface follows the magnetic field contour. Contouring of the anode to the magnetic field was claimed by Tikhonov to improve performance,[4,17] and experimentally verified by Tahara.[36] In order to describe the degree to which the anode geometry matches the magnetic field topology, we first model the magnetic field using the Biot-Savart law for a solenoid,

$$B(z) = B_{\mathrm{a0}} \frac{r_{\mathrm{B}}^3}{\left(r_{\mathrm{B}}^2 + z^2\right)^{3/2}}, \tag{12}$$

where z is the axial distance from the end of the solenoid. To a reasonable approximation, an anode which is contoured to the magnetic field is one for which the magnetic flux through the anode throat, Φ_{a0}, is equal to the flux through the anode exit plane, Φ_{ae}. We define the nondimensional value

$$\bar{\Phi} = \frac{\Phi_{\mathrm{ae}}}{\Phi_{\mathrm{a0}}} = \frac{r_{\mathrm{ae}}^2 r_{\mathrm{B}}^3}{r_{\mathrm{a0}}^2 \left(r_{\mathrm{B}}^2 + l_{\mathrm{a}}^2\right)^{3/2}}, \tag{13}$$

where l_{a} is the length of the anode between the throat and the exit plane. Physically, $\bar{\Phi} = 1$ represents an anode that is contoured to the magnetic field, while $\bar{\Phi} > 1$ represents an anode that diverges more rapidly than the magnetic field.

III. Data Catalogued

In order to compare predicted performance with experimental results, we require data for which a number of parameters have been recorded. We performed a thorough survey of the literature and collected all data which included measurements of each of the following: thrust (T), electrode current (J), electrode voltage

(V), magnetic field strength (B_{A}), propellant, mass flow rate $(\dot{m})$, background pressure (p_{b}), inner and outer solenoid radii (r_{Bi} and r_{Bo}), and electrode geometry. The electrode geometry recorded includes the anode length, l_{a}, the anode radius at the throat or backplate, r_{a0}, the anode radius at the exit plane, r_{ae}, the cathode length, l_{c}, and the cathode radius, r_{c}, as is illustrated in Fig. 2.

For some configurations, multiple anode lengths were recorded as defined by distinct changes in contour (eg. Fig. 2 (c), (e), and (f)), here denoted as l_{a1} and l_{a2}. Some configurations feature a change in contour, but the site of propellant injection implies the dominance of the exit region and so only the exit length is recorded (eg. Fig. 2 (b)). If thrust error and electrode material were reported, that information was also recorded. If the magnetic field strength was reported at multiple locations, that recorded in the database is from the tip of the cathode. Where measurements were not explicitly listed, they were deduced if at all possible (eg. if thrust, efficiency, and current are known, the voltage can be deduced).

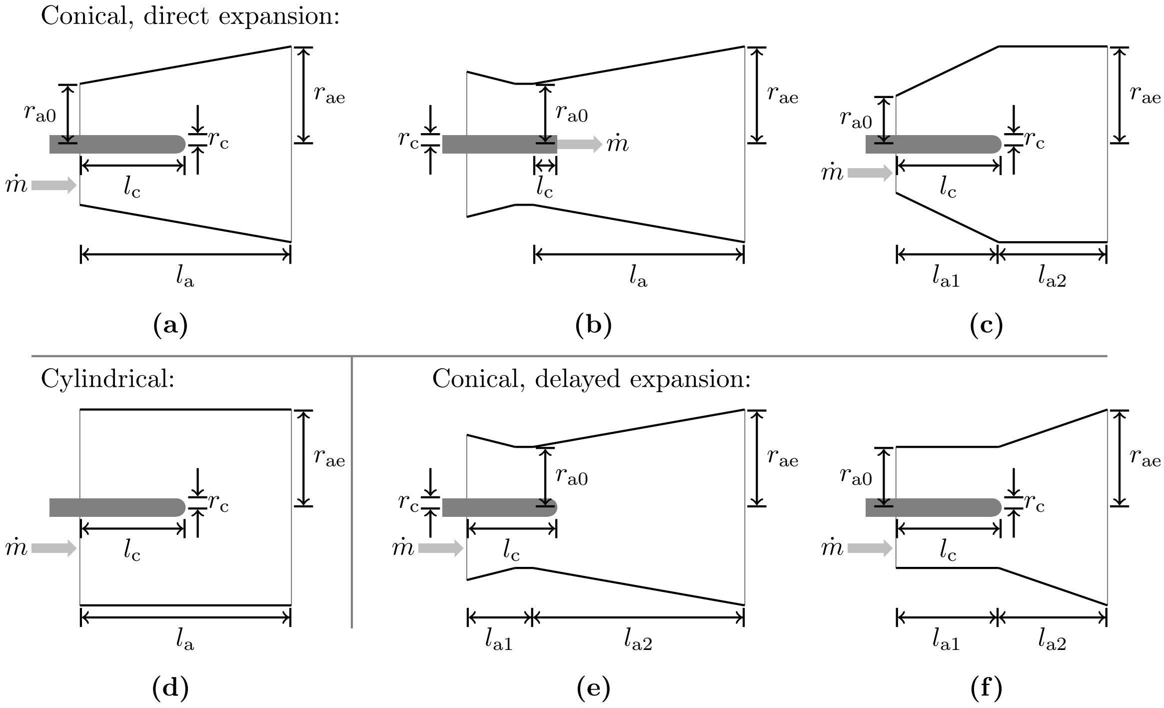

Figure 2: Characterization of the geometry for each of the thrusters in this study.

Measurements that were made using multiple species simultaneously were not recorded. Also omitted were thrusters using configurations that are not conducive to use with the thrust models of interest, such as rectangular MPDTs,[37,38] the hybrid plasma thruster,[39] and thrusters using permanent magnets.[40]

More than 2600 thrust measurements and corresponding operating parameters were collected in this survey. Each thruster for which we have data is listed in Appendix C, along with typical operating conditions and citations for the gathered data. The full data collection can be accessed online.[41]

IV. Determination of Data Validity

It has been demonstrated previously that background pressures above a given threshold influence thruster performance.[23,42–48] A comprehensive review of this influence is provided in Ref. 49. Because only two thrusters[43,47,48] have data for which background pressure is shown to have no influence, we need to determine which of the collected measurements are affected by high background pressures.

An interpolation of the data collected to determine background pressure effects in Ref. 48 is shown in Fig. 3. We see that there are three distinct regimes denoted here as I, II, and III. Region I shows no influence of background pressure on thrust, indicating that below a given threshold, just under 1 mTorr in this case, the thrust data are representative of that expected for an actual spacecraft. Region II shows a decrease in thrust. This is due to collisions in the plume that interfere with the expansion through the magnetic

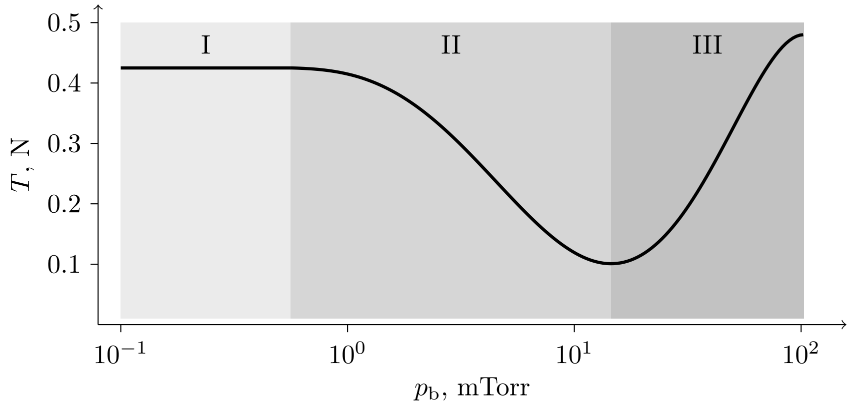

Figure 3: Typical thrust variation as a function of background pressure with three distinct regimes.

nozzle.[42, 46, 50] In Region III, the thrust increases with pressure due to mass entrainment in the thruster, effectively increasing the mass flow rate.[42, 46, 50]

Cann et al. performed the same test as that in Ref. 48 on the same model thruster, but using potassium propellant instead of sodium.[47] Again, they showed that the thrust was unaffected by background pressure up to 1 mTorr. The only other data that show a distinctly level region were in Ref. 43, where effects of pressure on thrust were minimal up to 0.9 mTorr with argon propellant.

Sovey et al.[42] report 0.3 mTorr as a safe upper-limit for operation without facility pressure effects on performance. However, their primary metric for this determination was the thrust-to-power ratio measured as a function of background pressure. We make the distinction that we are interested only in the effects of pressure on *thrust* because voltage is not a variable in the thrust models under review. Based on the limited thrust data available, it appears that 1 mTorr is a sufficiently low pressure to minimize any influence on thrust, however we separately analyzed the data collected at or below 0.1 mTorr and that collected at or below 1 mTorr with the results given in Table 1 and Fig. 6. Performance across a wide range of facility pressures is given in Fig. 5.

V. Method

Using the database, while excluding data collected at high pressure, we could compare the prediction of any given model with any single given measurement, however we seek a method that will allow us to make a comparison en masse over a large and varied parameter space. We have developed a method by which a model's ability to predict measurement as a function of a controllable parameter can be tested. Furthermore, due to the previously stated discrepancies between the prediction of the Maecker formula and measurement, we apply this method without invoking self-field or gasdynamic thrust models (except where implicitly prescribed by a particular applied-field model) by limiting our analysis to measurements for which the applied-field component is dominant.

A. Comparison Method

To evaluate the degree to which each model predicts measurement, we nondimensionalize each prediction for a given set of parameters with the measured thrust,

$$\bar{T}_\mathrm{model} = \frac{T_\mathrm{model}}{T_\mathrm{measured}}. \tag{14}$$

A perfect model would yield $\bar{T} = 1$ for every data point, however a more predictive model is one that predicts trends rather than magnitude, and so we normalize the nondimensional thrust for each model such that

$$\hat{\bar{T}}_\mathrm{model} = \frac{\bar{T}_\mathrm{model}}{\left\langle \bar{T}_\mathrm{model} \right\rangle}, \tag{15}$$

where the bra–ket notation indicates an average over all measurements.

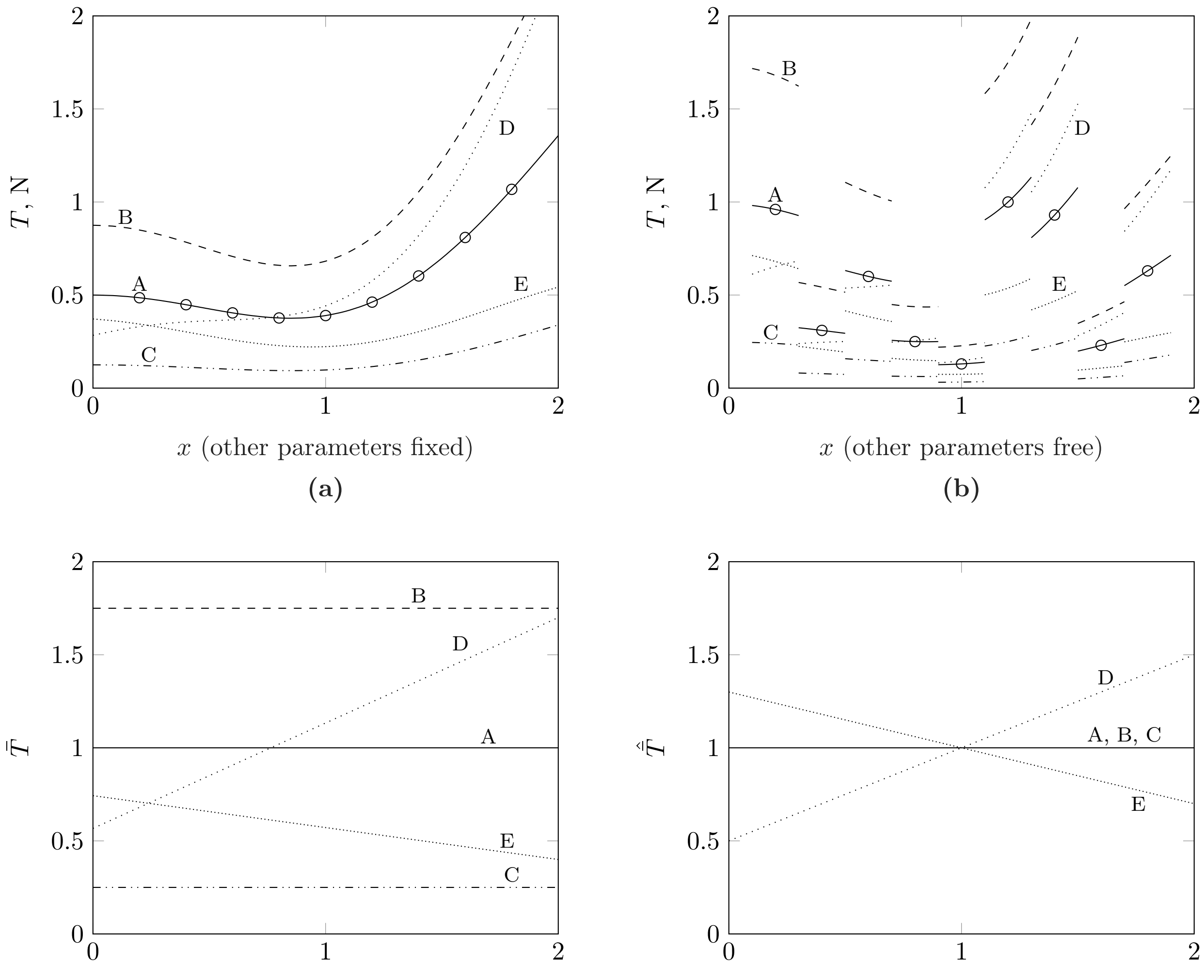

(a) (b)

(c) (d)

Figure 4: In (a), examples of how models A–E of T vary as a function of the arbitrary parameter x compared to data where all other parameters are held fixed. In (b), the same is shown except that parameters other than x are different for each measurement. Bottom, examples of how $\bar{T}$ and $\hat{\bar{T}}$ vary for those same models, showing only models D and E have incorrectly described the dependence of T on x.

Figure 4 shows five examples of what this procedure might produce for a given model as a function of the arbitrary parameter x. Figure 4 (a) is what one would typically use to illustrate that a model correctly describes thrust as a function of x when measurements are made with all other parameters held fixed. Because different measurements across the database have different parameters held fixed, (b) is more representative of what this same method would yield in our case. In both (a) and (b), it is difficult to compare one model's effectiveness to another, and we can only tell that model A consistently predicts the measured value. The nondimensionalization and normalization procedures applied in (c) and (d) clarify how well each model predicts the magnitude of thrust, and thrust scaling, respectively, as a function of x. From (c) and (d), we are able to deduce the following about models A–E:

A. The model predicts the magnitude of the measurement, as well as how thrust varies as a function of x.

B. The model overpredicts thrust, but correctly predicts how thrust varies as a function of x.

C. The model underpredicts thrust, but correctly predicts how thrust varies as a function of x.

D. The model overpredicts thrust, and predicts a different thrust dependence on x than that which is represented by the data.

E. The model underpredicts thrust, and predicts a different thrust dependence on x than that which is represented by the data.

Because normalization decreases the slope of D, but increases the slope of E, we are able to compare the predictions of the two models. Otherwise, models that underpredict thrust will tend to have smaller slopes, as is illustrated by Fig. 4 (c).

We apply this methodology to examine how $\hat{\hat{T}}$ scales as a function of each controllable parameter of interest. In most cases, there are not enough data points for us to determine any high-order or periodic dependence of $\hat{\hat{T}}$ on a given controllable parameter, so we seek only to determine if $\hat{\hat{T}}$ is monotonically increasing or decreasing. Such behavior indicates that the thrust dependence is not captured by the model of interest.

For each parameter investigated, we make a linear fit of $\hat{\hat{T}}$ as a function of that parameter using a χ^2 test for goodness of fit. We weight each measurement by the inverse of the square of the error on that measurement. If the fit function for the parameter has a slope, and if the 95% confidence interval on that slope does not include 0, we conclude that the model over- or underpredicts as a function of that parameter.

The database includes two types of controllable parameters: those that are discrete, such as geometrical terms, for which there are relatively few values recorded, and those that are continuous, such as current. For simplicity, the figures show only the mean $\hat{\hat{T}}$ value for each value of the discrete parameters, with error bars denoting the interquartile region. However, the linear fit of $\hat{\hat{T}}$ is to the total dataset as it is for continuous parameters.

B. Filtering Method

In order to test the various models of the applied-field thrust component, we filter the thrust database for measurements for which that component dominates. To filter the data, we use the Tikhonov et al. model of the applied-field thrust, which has been most verified experimentally,[5, 9, 51, 52] to establish whether the applied-field component is significant. If the prediction of the Tikhonov et al. model for a set of parameters is found to be a significant fraction of the thrust measurement, we can assume that the applied-field thrust component is dominant, and the models should all closely match the data, whether they predict the applied-field component or the sum of several components.

Due to the demonstrated effects of background pressures over 1 mTorr, we have the additional requirement that all data analyzed was gathered at or below this pressure except for our investigation of background pressure effects, as is noted in Table 1 and Figs. 5 and 6. We chose the thresholds

$$\frac{T_{\text{Tikhonov}}}{T_{\text{measured}}} > 0.9 \text{ and } p_{\text{b}} \leq 1 \text{ mTorr}. \tag{16}$$

C. Application of Data to Models

Each of the models depends on r_{a}, but many thrusters have flared anodes for which we need to determine which anode radius to use. In all cases where the models do not specify otherwise, we use the average radius, $r_{\text{a}} = {}^{(r_{\text{a0}}+r_{\text{ae}})}/_{2}$. Similarly, because solenoids have both inner and outer radii, we define $r_{\text{B}} = {}^{(r_{\text{Bi}}+r_{\text{Bo}})}/_{2})$. We use the total anode length (either l_{a} or $l_{\text{a1}} + l_{\text{a2}}$) except in Eq. 13 for parameter $\bar{\Phi}$, where l_{a2} is used for delayed expansion conical anodes. The cathode length is determined by the propellant injection location as is described in Sec. III. For B_{A}, we use the magnetic field strength that is reported at the tip of the cathode.

Error was not reported for all measurements. In order to lessen the bias on our conclusions by measurements without reported error, we assume the error on these values to be 15% of the measurement. This percentage is the largest reported error in the analyzed data.

VI. Results and Discussion

A. Background Pressure Effects

We first examine the effects of background pressure on all measurements for which ${}^{T_{\text{Tikhonov}}}/{}_{T_{\text{measured}}} > 0.9$. Fig. 5 shows how $\hat{\bar{T}}_{\text{Tikhonov}}$ behaves as a function of background pressure. We fit $\hat{\bar{T}}\left(\log p_{\text{b}}\right)$ with a moving average over ${}^{1}/{}_{10^{\text{th}}}$ the span of $\log(p_{\text{b}})$. Data outside six mean absolute deviations is ignored.

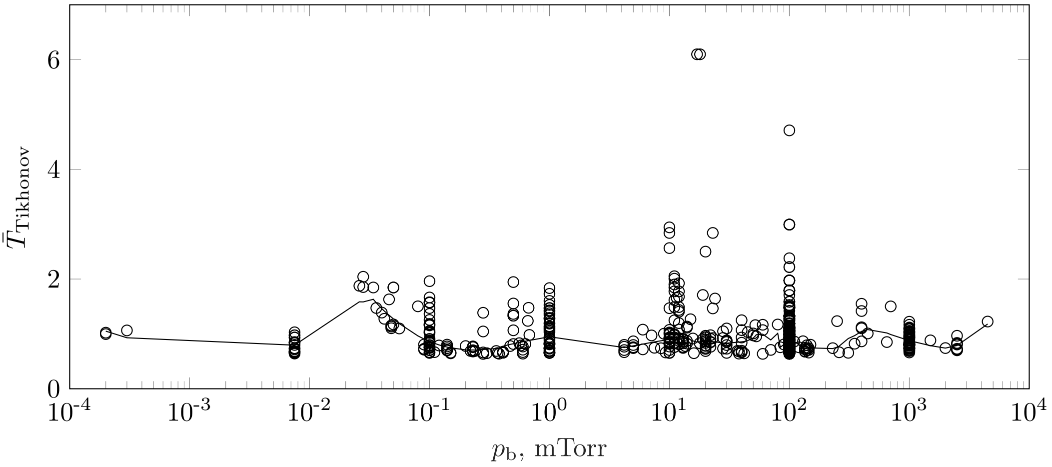

Figure 5: All data for which $\bar{T}_{\text{Tikhonov}} > 0.9$ as a function of background pressure. There is no upward trend between 1 and 10 mTorr despite the observation of such a trend for data gathered in Refs. 43, 47, 48.

Despite the effects of background pressure on thrust demonstrated by Refs. 43,47,48, we see no significant upward or downward trend in the behavior of $\hat{\bar{T}}$ as a function of p_{b}. We attribute this observation to the symmetrical behavior illustrated in Fig. 3. We cannot assume, based on the results from only two thrusters, that the minimum on the border of regions II and III is at a fixed pressure for all thrusters and facilities. Furthermore, we do not have any data with all parameters other than p_{b} fixed that spans beyond region III with which to speculate about behavior in higher pressure regimes. The only conclusion we can draw from Fig. 5 is that the pressure at which thrust is minimized is not universal across facilities, otherwise we would observe a local maximum about that pressure. Since there is no consistent pressure threshold below which data can be considered valid, verification of the absence of background pressure effects needs to be more highly prioritized in future experimental publications.

Because most measurements for a given thruster are recorded at a constant background pressure, we examine, in Fig. 6, the average $\hat{\bar{T}}$ value for each thruster operating at or below 0.1 mTorr, and for each thruster operating in the range of 0.1 mTorr $< p_{\text{b}} \leq 1$ mTorr. We observe different average $\hat{\bar{T}}$ values for each thruster, but no correlation with pressure. Furthermore, Table 1 shows that for most models the relative standard deviation, $\hat{s}$, of the average nondimensionalized prediction, $\left\langle\bar{T}\right\rangle$, changes very little when the higher pressure data (≤ 1 mTorr) is included in the analysis. This observation justifies our use of data gathered at ≤ 1 mTorr for all of the following results.

B. Analysis of Existing Models

In Table 1, we show the average nondimensionalized prediction, $\left\langle\bar{T}\right\rangle$, and the relative standard deviation, $\hat{s}$, for each model. We see that the Albertoni et al. model comes closest to predicting the average measurement value. This is as expected, since this model scales the Fradkin et al. model by a constant, k, such that $k\left\langle\bar{T}_{\text{Fradkin}}\right\rangle = 1$. Because $\left\langle\bar{T}_{\text{Fradkin}}\right\rangle$ was found by Albertoni et al. using a different dataset than is used here, we find a different average value, which results in an average overprediction of 14% by their model. The Mikellides and Turchi model also comes close to predicting the measured value, but was limited to a smaller dataset due to its inability to accommodate recessed cathodes.

The models of Herdrich et al. and Mikellides and Turchi yield the smallest relative standard deviation. The model by Sasoh and Arakawa yields the largest relative standard deviation. The range of values reported

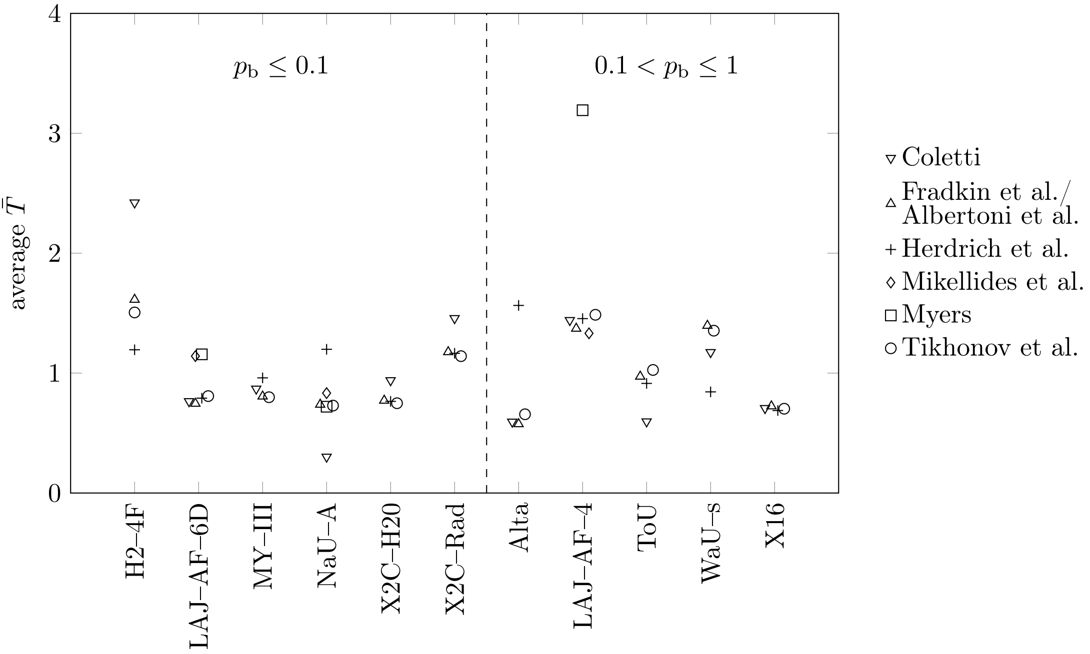

Figure 6: The average $\hat{\bar{T}}$ value for each thruster in the specified background pressure regimes (in mTorr) is shown for each model. There are larger differences in individual thrusters than in distinct pressure regimes.

Table 1: Mean $\bar{T}$ value and relative standard deviation ($\hat{s}$) for each model.

p_{b} (mTorr)		Albertoni et al.	Coletti	Fradkin et al.	Herdrich et al.	Mikellides et al.	Myers	Sasoh et al.	Tikhonov et al.
≤ 1	$\langle \bar{T} \rangle$	1.14	2.40	4.54	1.33	0.86	5.08	0.51–9.7	1.41
	$\hat{s}$	0.38	0.67	0.38	0.29	0.29	0.48	0.82–3.1	0.35
≤ 0.1	$\langle \bar{T} \rangle$	1.24	3.27	4.97	1.42	0.75	5.96	0.66–8.7	1.49
	$\hat{s}$	0.38	0.53	0.38	0.27	0.23	0.37	0.64–3.5	0.36

in Table 1 for this model correspond to the temperatures and exhaust velocities yielding the smallest and largest relative standard deviations. For data gathered at ≤ 1 mTorr, we found the smallest relative standard deviation corresponds to $\mathcal{T}_{\mathrm{e}} = 0.9$ eV and $u_{\mathrm{ex}} = 0.8$ km/s. The largest relative standard deviation corresponds to $\mathcal{T}_{\mathrm{e}} = 1.5$ eV and $u_{\mathrm{ex}} = 86$ km/s. We conclude that more developed models are needed to determine all input values based on controllable parameters.

The results of our tests for the missed dependencies of each model are given in Table 2. By missed dependency, we mean the degree to which a model over- or underpredicts thrust as a function of a given parameter. Examples of the analyses are shown in Figs. 7–9, 11, and 12. For most models, few missed dependencies were confirmed within a 95% confidence interval. The exceptions are the Myers and Mikellides and Turchi models, which each miss dependencies on each parameter tested, however some of the geometric parameters are likely correlated, since larger thrusters tend to be larger in all dimensions. The Sasoh and Arakawa model also has many missed dependencies. The values for this model correspond to the minimum and maximum slopes found using the full range of possible ion temperatures and exhaust velocities. Due to the wide range of possible slopes for most parameters, this model is excluded from all figures. The models of Tikhonov et al., Fradkin et al., and Albertoni et al. have the fewest missed dependencies.

The largest deviations between prediction and experiment over the domain for which we have data occur for the dependence of $\hat{\bar{T}}$ on electrode radii. Figure 7 shows the fit function for $\hat{\bar{T}}(r_{\mathrm{a}})$ for each model. While the Herdrich et al. model was derived specifically to capture the thrust dependence on anode radius missed

Table 2: Calculated slope of linear fit of $\bar{\hat{T}}$ of each model for each parameter using data gathered at ≤ 1 mTorr. Entries with a 95% confidence bounds of a non-zero slope are shown in bold.

	Coletti	Fradkin et al./ Albertoni et al.	Herdrich et al.	Mikellides et al.	Myers	Sasoh et al.	Tikhonov et al.
r_c (cm^{-1})	−0.23	−0.18	0.45	**−1.2**	**−3.4**	−0.91, **−0.0066**	−0.19
l_c (cm^{-1})	−0.033	−0.016	0.0089	**−0.034**	**−0.073**	**−0.065**, 1.4e−8	−0.016
r_a (cm^{-1})	−0.068	−0.059	0.18	**−0.17**	**−0.47**	−0.25, **−0.0012**	−0.074
l_a (cm^{-1})	−0.027	−3.5e−4	0.019	**−0.022**	**−0.063**	**−0.012**, **0.066**	−0.0044
r_B (cm^{-1})	−0.073	−0.049	0.098	**−0.20**	**−0.58**	−0.24, **−0.0012**	−0.050
M (u^{-1})	**0.0021**	**0.0060**	**0.0057**	**−0.0081**	**−0.039**	**−0.0033**, 2.5e−4	**0.0063**
ϵ_i (eV^{-1})	0.0033	−0.018	**−0.018**	**−0.026**	**−0.075**	5.6e−5, **0.023**	−0.019
J (kA^{-1})	**0.22**	0.063	**0.12**	**1.1**	**3.7**	2.2e−4, **1.1**	0.053
B (T^{-1})	**−0.36**	0.39	0.40	**1.3**	**3.9**	**−0.61**, **0.30**	0.41
$\dot{m}$ (s/g)	0.40	0.023	0.23	**9.8**	**24**	−2.0, **0.57**	−0.026
$\bar{\Phi}$	0.0026	0.0051	−0.0021	**0.43**	**1.2**	**1.3e−4**, 0.0073	0.0057
$r_\mathrm{a}/r_\mathrm{c}$	−0.024	0.025	0.089	**−0.21**	**−0.61**	**−0.11**, 0.36	−0.019
$l_\mathrm{c}/l_\mathrm{a}$	0.0017	−0.049	−0.014	**0.15**	**0.42**	**−0.12**, 8.9e−8	−0.041
$r_\mathrm{ae}/r_\mathrm{a0}$	0.0075	0.025	−0.018	**−0.55**	**−1.6**	**5.9e−4**, 0.041	0.030
$l_\mathrm{c}/r_\mathrm{c}$	−0.018	−0.011	0.0031	**−0.026**	**−0.057**	**−0.030**, 8.5e−9	−0.010
$l_\mathrm{a}/r_\mathrm{a}$	−0.16	0.035	−0.022	**−0.079**	**−0.23**	**−0.068**, 0.080	0.040

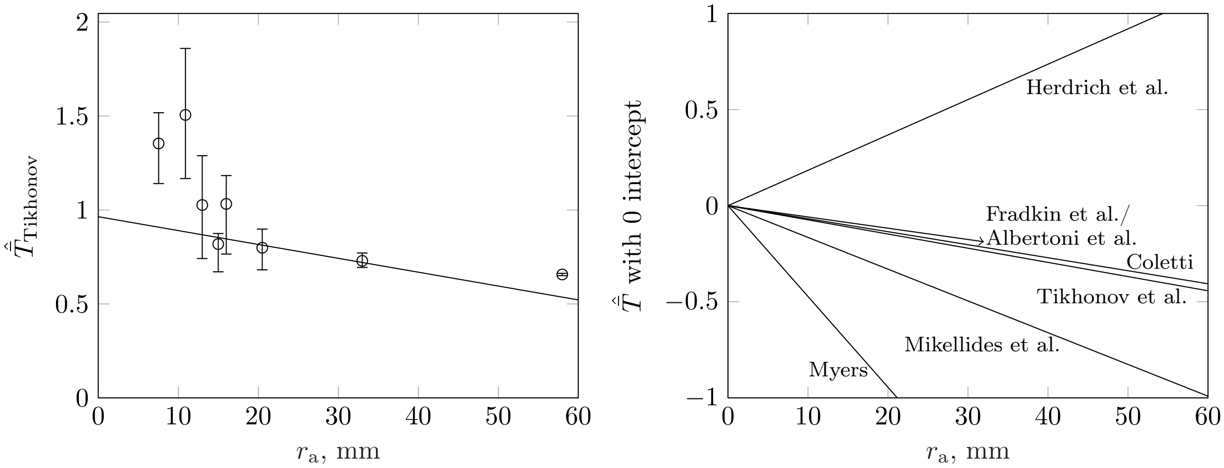

Figure 7: Left, the mean value of $\bar{\hat{T}}_\mathrm{Tikhonov}$ as a function of $r_\mathbf{a}$ is shown with error bars representing the interquartile region. Right, the linear fits for each model are shown with a common intercept. All data was taken at or below 1 mTorr.

by the Tikhonov et al. model,[5] it overpredicts the thrust because the empirical model of Herdrich et al. was made using a different dataset than that used here. Because the slope changes substantially depending on which dataset is used, there is likely either a more complicated dependence on anode radius than can be described by a power law fit, or an additional unknown parameter upon which thrust depends. While $\bar{\hat{T}}_\mathrm{Tikhonov}$ and $\bar{\hat{T}}_\mathrm{Fradkin}$ have similar slopes as a function of anode radius, we see in Fig. 8 that the $\bar{\hat{T}}$ values diverge as a function of our nondimensionalized electrode radius, ${}^{r_\mathrm{a}}/_{r_\mathrm{c}}$, indicating that the electrode aspect ratio is also a relevant parameter to thrust scaling.

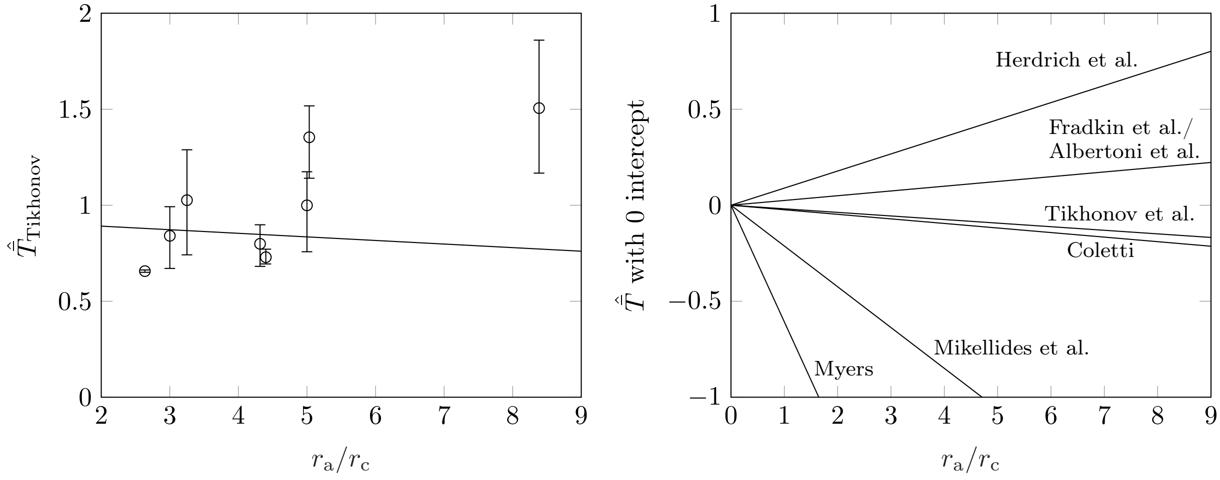

Figure 8: Left, the mean value of $\hat{\bar{T}}_{\text{Tikhonov}}$ as a function of $r_\mathbf{a}/r_\mathbf{c}$ is shown with error bars representing the interquartile region. Right, the linear fits for each model are shown with a common intercept. All data was taken at or below 1 mTorr.

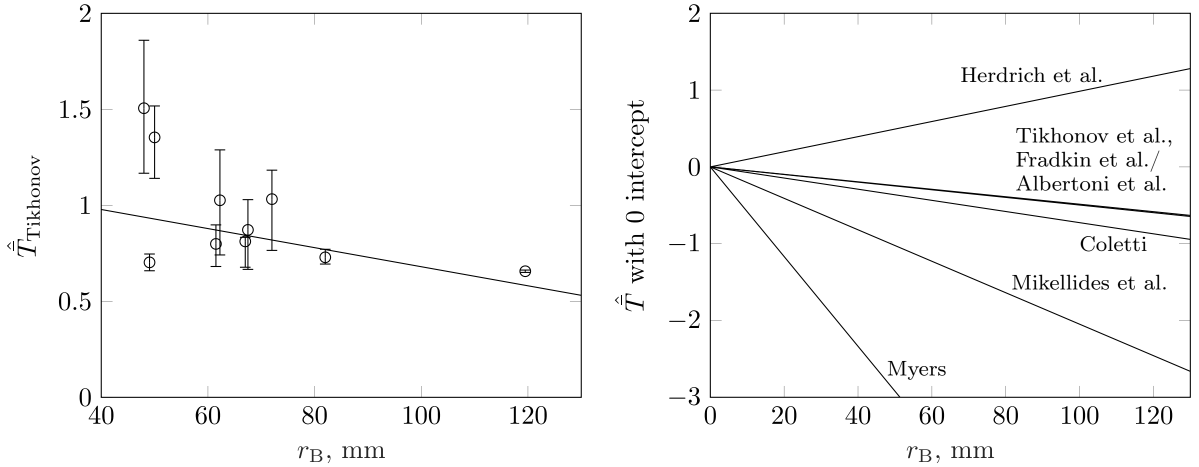

Figure 9: Left, the mean value of $\hat{\bar{T}}_{\text{Tikhonov}}$ as a function of $r_\mathbf{B}$ is shown with error bars representing the interquartile region. Right, the linear fits for each model are shown with a common intercept. All data was taken at or below 1 mTorr.

There is also a substantial deviation between prediction and experiment as a function of the solenoid radius (Fig. 9). Only the models of Sasoh and Arakawa and Coletti attempt to capture the influence of this parameter, however we observe nearly identical behavior in Figs. 7 and 9. This consistent behavior despite a change in prediction indicates that there is a correlation between anode and solenoid radii, which we show to be the case in Fig. 10. Tests performed with different solenoid radii for a fixed anode radius[36] and with different anode radii for a fixed solenoid radius[43] show that thrust increases with each of these parameters.

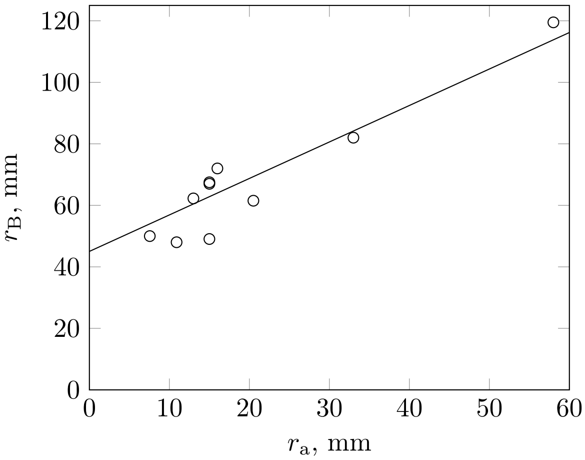

Figure 10: Correlation between solenoid and anode radii for data taken at or below 1 mTorr.

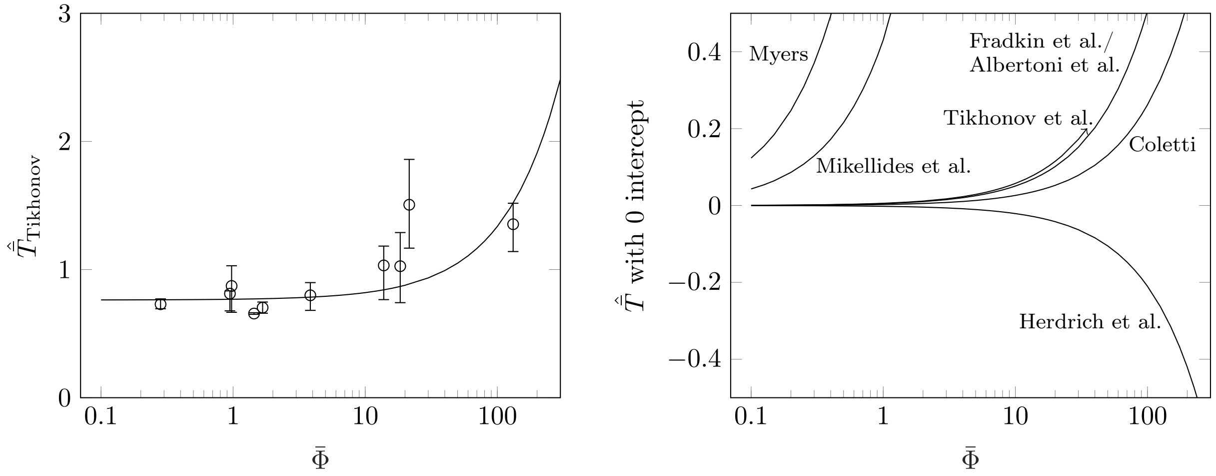

Figure 11: Left, the mean value of $\hat{\bar{T}}_\mathrm{Tikhonov}$ as a function of $\bar{\Phi}$ is shown with error bars representing the interquartile region. Right, the linear fits for each model are shown with a common intercept. All data was taken at or below 1 mTorr.

Because the correlation between anode and solenoid radii makes it difficult to determine which of these variables contributes to thrust, we look at $\bar{\Phi}$, which incorporates both parameters into a single one. We see in Fig. 11 that most models deviate substantially from measurement as a function of this variable, where large values typically result in overpredictions.

Most models correctly describe thrust dependence on current, magnetic field strength, and mass flow rate, and even those with missed dependencies typically have slopes corresponding to small changes in $\hat{\bar{T}}$ over the domain of a given parameter. However, we find that the Myers model overpredicts thrust dependence on each of these parameters. By comparing T_Myers to T_Tikhonov, we see that this overprediction must be a result of correlations with the electrode aspect ratio and/or the cathode length. The Mikellides and Turchi model also overpredicts thrust dependence on J, B_A, and $\dot{m}$, but $T_\mathrm{Mikellides}$ is not easily comparable with other

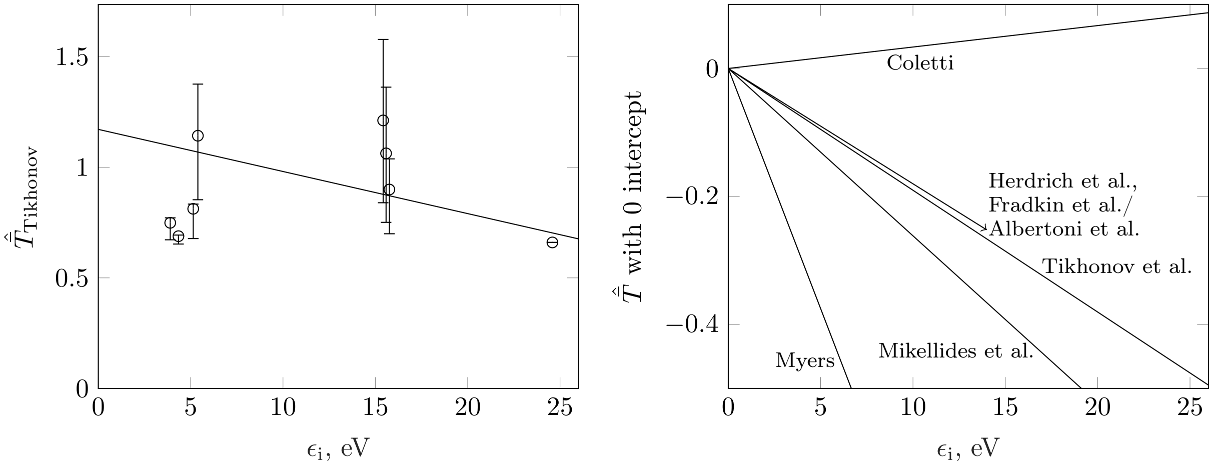

Figure 12: Left, the mean value of $\hat{\hat{T}}_{\text{Tikhonov}}$ as a function of ϵ_{i} is shown with error bars representing the interquartile region. Right, the linear fits for each model are shown with a common intercept. All data was taken at or below 1 mTorr.

models. Nonetheless, while the Mikellides and Turchi model yields one of the smallest relative standard deviations and on average comes close to predicting the magnitude of a measurement, it fails to predict performance as a function of the controllable parameters of interest.

In implementing the model of Mikellides and Turchi, we assumed that the ionization factor, $\bar{Y} = 1$. We expect this factor to decrease within increasing ionization energy, which would increase the slope of $\hat{\hat{T}}_{\text{Mikellides}}$ in Fig. 12. However, the agreement between prediction and measurement for the models of Coletti, Fradkin et al., and Tikhonov et al. which predict no dependence, suggests that while ionization energy affects the electrode voltage,[49] it does not strongly influence the generated thrust. We see in Fig. 12 that $\hat{\hat{T}}_{\text{Tikhonov}}$ is decreasing slightly, whereas we would expect a positive slope if alkali propellants benefited thrust generation.

VII. Π-product-corrected Model

We have shown that several of the existing models fail to describe the data as a function of specific controllable parameters, while others seem to describe the data despite making different predictions. We now derive a new model empirically by assuming we know each of the parameters upon which the thrust depends.[53] Using this empirical model, we will attempt to shed light on the physical mechanism responsible for the disagreement between existing models and measurement.

A. Method

We assume the general functional expression for the applied-field component of thrust,

$$T_{\text{AF}} = f\left(J, B_{\text{A}}, r_{\text{a0}}, r_{\text{ae}}, l_{\text{a}}, r_{\text{c}}, l_{\text{c}}, r_{\text{B}}\right). \tag{17}$$

There are nine parameters and four independent dimensions (mass, length, time, and charge), so per the Buckingham Π theorem, we can reduce this function to five nondimensional Π products. We choose the parameters

$$\Pi_1 = \frac{T_{\text{AF}}}{J B_{\text{a}} r_{\text{a}}}, \tag{18}$$

$$\Pi_2 = \bar{\Phi}\left(r_{\text{a0}}, r_{\text{ae}}, l_{\text{a}}, r_{\text{B}}\right), \tag{19}$$

$$\Pi_3 = \frac{r_{\text{a}}}{r_{\text{c}}}, \tag{20}$$

$$\Pi_4 = \xi + \frac{l_c}{l_a}, \text{ where } \xi \text{ is a constant and} \tag{21}$$

$$\Pi_5 = \frac{r_{ae}}{r_{a0}}. \tag{22}$$

Using these Π products, we can derive a formula by assuming the general form

$$T_{AF} = kJB_a r_a \Pi_2^{\kappa_2} \Pi_3^{\kappa_3} \Pi_4^{\kappa_4} \Pi_5^{\kappa_5}, \tag{23}$$

where κ_i is the power for the i^{th} Π product found by fitting to the data, and k is a constant such that $\langle \bar{T}_{AF} \rangle = 1$. We solve for κ_2 by assuming that κ_3, κ_4, and $\kappa_5 = 0$, and minimizing the standard deviation of $\hat{\bar{T}}_{AF}$. Then, knowing κ_2, we can solve for κ_3 continuing the assumption that κ_4 and $\kappa_5 = 0$, and so on until κ_5 is determined. This method provides an approximate value for each κ_i, which can be improved with subsequent iterations until the κ values converge.

Since ${}^{l_c}/_{l_a}$ can be negative, and since we require that $T_{AF} > 0$, we choose a constant ξ such that $\min(\Pi_4) > 0$. $\xi = 10$ is used for all analyses.

B. Results

We show our empirical solution to T_{AF_j} in Table 3, where the index j indicates the number of corrections to the initial solution using only Π_1. We see that the relative standard deviation improves markedly after one correction, but then converges rapidly to $\hat{s} = 0.267$. Table 4 gives the slopes of $\hat{\bar{T}}_{AF}$ as a function of each parameter for each iteration of the Π-product-corrected model. The initial slopes are the same as those for the Tikhonov et al. model since $\hat{\bar{T}}_{AF_0} = \hat{\bar{T}}_{\text{Tikhonov}}$. The number of parameters the model fails to capture decreases with each iteration until at last only one is remaining.

Table 3: Evolution of model over successive iterations of Π products.

Iteration	Model	$\hat{s}$
T_{AF_0}	$0.14JBr_a$	0.350
T_{AF_1}	$0.16JB_A r_a \bar{\Phi}^{-0.13}$	0.249
T_{AF_2}	$0.22JB_A r_a \bar{\Phi}^{-0.13} \left({}^{r_a}/_{r_c}\right)^{-0.20}$	0.247
T_{AF_3}	$0.99JB_A r_a \bar{\Phi}^{-0.13} \left({}^{r_a}/_{r_c}\right)^{-0.20} \left(10 + {}^{l_c}/_{l_a}\right)^{-0.67}$	0.229
T_{AF_4}	$1.14JB_A r_a \bar{\Phi}^{-0.13} \left({}^{r_a}/_{r_c}\right)^{-0.30} \left(10 + {}^{l_c}/_{l_a}\right)^{-0.67}$	0.228

We found Π_5 to be unnecessary to further improve the agreement with measurement, and so left $\kappa_5 = 0$. The only κ value we solved for more than once is κ_3, but we found that the relative standard deviation was only marginally improved. All slopes are 0 within the certainty of the data except for as a function of M, which was not included in our original list of independent variables. This parameter makes the final model underpredict thrust by $< 0.3\%$ per u. Adding M to our list of variables requires an additional variable for normalization. Subsequently, a new solution requires two additional Π products. We deem the added complexity insufficiently warranted by such a weak dependence.

The results of the Π-product-corrected model are shown in Fig. 13. We see excellent agreement between prediction and measurement across five orders of magnitude.

C. Physical Interpretation

The relative magnitudes of each of the described Π products indicates their relative importance. Aside from the already established $JB_A r_a$ scaling, $\bar{\Phi}$ is dominant, with the nondimensional electrode radius and length serving only as minor correction terms. We previously stated that $\bar{\Phi} > 1$ means that the anode diverges more rapidly than the applied magnetic field, but we expect this divergence to increase voltage (due to increased resistance across the magnetic field) rather than decrease thrust. However, a magnetic field that

Table 4: Calculated slope of linear fit to $\hat{\hat{T}}$ for each iteration of the Π-product-corrected model using data gathered at ≤ 1 mTorr. Entries with a 95% confidence bounds of a non-zero slope are shown in bold.

	$\hat{\hat{T}}_{\mathrm{AF}_0}$	$\hat{\hat{T}}_{\mathrm{AF}_1}$	$\hat{\hat{T}}_{\mathrm{AF}_2}$	$\hat{\hat{T}}_{\mathrm{AF}_3}$	$\hat{\hat{T}}_{\mathrm{AF}_4}$
r_{c} (cm^{-1})	-0.19	0.088	0.11	0.087	0.099
l_{c} (cm^{-1})	-0.016	0.030	0.030	0.015	0.015
r_{a} (cm^{-1})	-0.074	0.052	0.044	0.039	0.033
l_{a} (cm^{-1})	-0.0044	0.0014	0.0029	0.0062	0.0066
r_{B} (cm^{-1})	-0.050	0.032	0.035	0.020	0.020
M (u^{-1})	**0.0063**	**0.0049**	**0.0053**	**0.0052**	**0.0053**
ϵ_{i} (eV^{-1})	-0.019	-0.017	-0.018	-0.017	-0.017
J (kA^{-1})	0.053	0.080	0.074	0.078	0.074
B (T^{-1})	0.41	0.36	0.39	0.38	0.38
$\dot{m}$ (s/g)	-0.026	0.12	0.085	0.10	0.081
$\bar{\Phi}$	0.0057	-0.0024	-0.0021	-0.0016	-0.0015
$r_{\mathrm{a}}/r_{\mathrm{c}}$	-0.019	0.048	0.015	0.020	0.0028
$l_{\mathrm{c}}/l_{\mathrm{a}}$	-0.041	0.068	0.081	0.029	0.033
$r_{\mathrm{ae}}/r_{\mathrm{a0}}$	0.030	-0.026	-0.022	-0.015	-0.013
$l_{\mathrm{c}}/r_{\mathrm{c}}$	-0.010	0.018	0.018	0.0082	0.0080
$l_{\mathrm{a}}/r_{\mathrm{a}}$	0.040	-0.045	-0.033	-0.018	-0.012

expands more slowly than the anode is effectively freezing the charged particles to a surface of constant flux, reducing the area over which the Lorentz force acts.

Using Eq. 12, and assuming the initial radius at $z = 0$ to be r_{a0}, we find this radius of constant flux at the anode exit plane to be

$$r_{\text{ae-}\Phi} = r_{\mathrm{a0}} \sqrt{\frac{\left(r_{\mathrm{B}}^2 + l_{\mathrm{a}}^2\right)^{3/2}}{r_{\mathrm{B}}^3}}. \tag{24}$$

We assume that there is some effective anode radius at the exit plane, $r_{\text{ae-eff}}$, such that $r_{\text{ae-}\Phi} \leq r_{\text{ae-eff}} \leq r_{\mathrm{ae}}$, for all $r_{\text{ae-}\Phi} \leq r_{\mathrm{ae}}$. The plasma within the anode volume is often collisional, and so we do not expect the charged particles to necessarily be completely frozen to an initial flux surface, but rather anticipate that they will expand to some point between the radius of constant flux and the anode radius at the exit plane, depending on the degree to which they are confined. The effective anode radius relevant to the Lorentz force is then

$$r_{\mathrm{eff}} = \frac{r_{\mathrm{a0}} + r_{\text{ae-eff}}}{2}, \tag{25}$$

where we approximate the flux surface as a cone (shown schematically in Fig. 14). The degree to which $r_{\text{ae-eff}}$ extends beyond $r_{\text{ae-}\Phi}$ can be expressed by the nondimensional value

$$\hat{r}_{\text{a-}\Phi} = \frac{r_{\text{ae-eff}} - r_{\text{ae-}\Phi}}{r_{\mathrm{ae}} - r_{\text{ae-}\Phi}}, \tag{26}$$

where $0 \leq \hat{r}_{\text{a-}\Phi} \leq 1$.

We do not expect a universal $\hat{r}_{\text{a-}\Phi}$ value to exist, since this term depends on the degree of confinement, which is a function of the gasdynamic and magnetic pressures, each of which varies as a function of the operating conditions. However, we do expect better agreement between prediction and experiment for intermediate values than for the extremes, since we assume that the plasma is collisional and that the magnetic field is restricting radially outward flow. By iterating over all possible $\hat{r}_{\text{a-}\Phi}$ values and solving for the relative standard deviation, $\hat{s}$, of $kJB_{\mathrm{A}}r_{\mathrm{eff}}/T_{\mathrm{measured}}$, we see in Fig. 14 that there is indeed a substantial

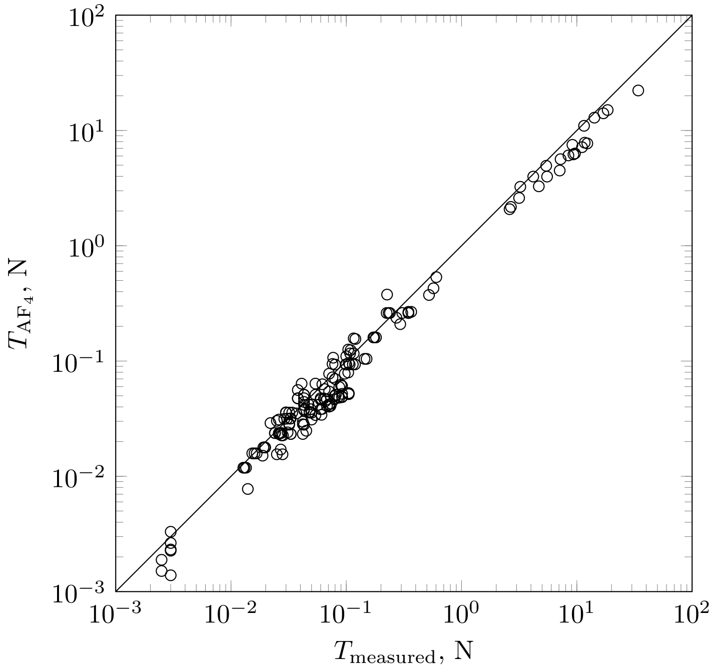

Figure 13: Comparison of T_{AF_4} prediction to measurement for data taken at or below 1 mTorr.

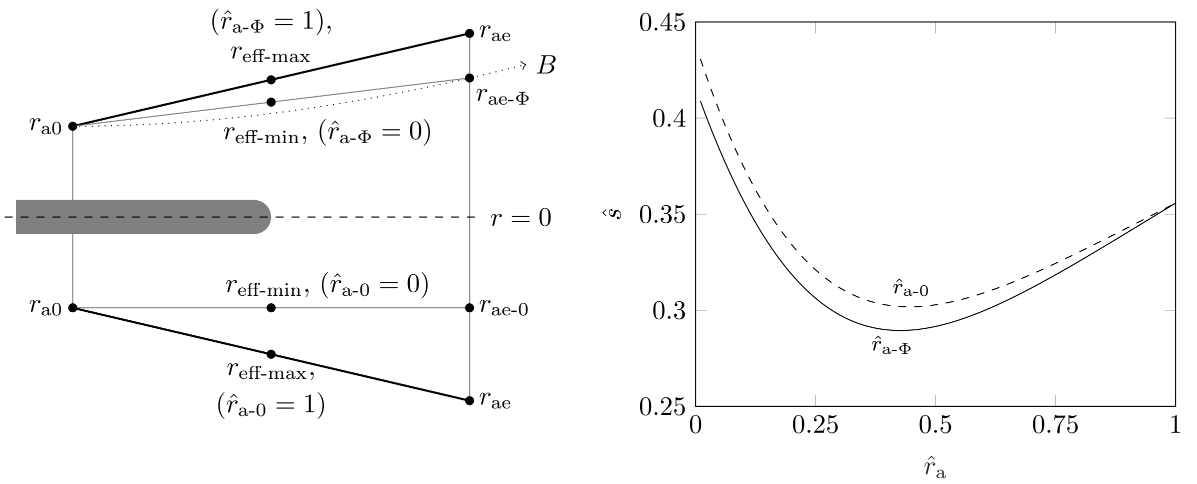

Figure 14: Left, the effective anode radii found using either the flux surface (top half) or the range of the physical anode (bottom half) are depicted schematically. Right, the relative standard deviation is shown as a function of $\hat{r}$ for $kJB_{\text{A}}r_{\text{eff}}/T_{\text{measured}}$. All data was taken at or below 1 mTorr.

decrease in the relative standard deviation for intermediate values of $\hat{r}_{\text{a-}\Phi}$, with a minimum of $\hat{s} = 0.289$ at $\hat{r}_{\text{a-}\Phi} = 0.43$.

So far, we have arbitrarily asserted that $r_{\text{a}} = \langle r_{\text{a0}}, r_{\text{ae}} \rangle$. In order to verify that the reduction in $\hat{s}$ for certain $\hat{r}_{\text{a-}\Phi}$ values is not actually due to this arbitrary choice, we perform the same iteration over all possible physical anode radii. For consistency, we define

$$\hat{r}_{\text{a-0}} = \frac{r_{\text{ae-eff}} - r_{\text{ae-0}}}{r_{\text{ae}} - r_{\text{ae-0}}}, \tag{27}$$

where $0 \leq \hat{r}_{\text{a-0}} \leq 1$, as depicted in Fig. 14. Again, we see improved agreement between model and prediction, but to a lesser extent than was was found using $\hat{r}_{\text{a-}\Phi}$. The best agreement is found at $\hat{r}_{\text{a-0}} = 0.45$, where $\hat{s} = 0.302$. The corresponding effective radius is less than 1/4 the distance between the radius at the throat and that at the exit plane rather than half as was initially assumed. However, 77% of the data used in this analysis are represented by magnetically restricted anodes, meaning we anticipate $r_{\text{ae-eff}} < r_{\text{ae}}$ based on our previous assertion that the area over which the Lorentz force acts is restricted. If instead we select only the data for which $r_{\text{ae-}\Phi} \geq r_{\text{ae}}$, the relative standard deviation decreases monotonically for increasing $\hat{r}_{\text{a-0}}$, and continues decreasing even if the domain is expanded until $r_{\text{eff}} = r_{\text{ae}}$.

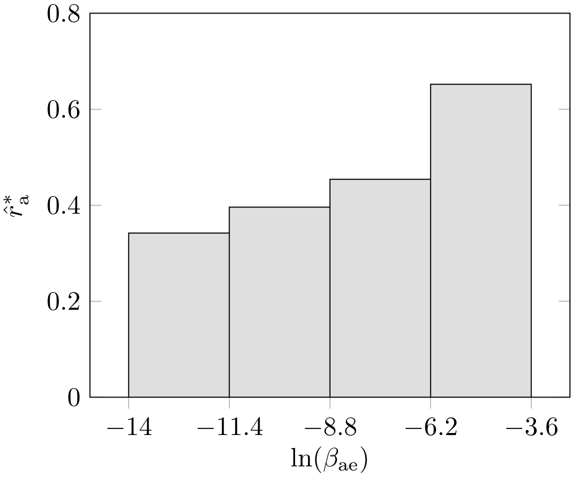

Figure 15: Bar plot showing the increase of the effective radius toward the anode as the ratio of the gasdynamic pressure to magnetic pressure increases. All data was taken at or below 1 mTorr.

We see further evidence that the effective area over which the Lorentz force acts is reduced by slowly diverging magnetic fields if we look at the ratio of gasdynamic to magnetic pressure at the anode exit plane,

$$\beta_{\text{ae}} = \frac{n_{\text{i}} k_{\text{B}} \mathcal{T}_{\text{i}}}{B_{\text{ae}}^2 / 2\mu_0}, \tag{28}$$

where k_{B} is the Boltzmann constant, n_{i} is the ion number density, and B_{ae} is the applied field strength at the anode exit plane. We assume $\mathcal{T}_{\text{i}} = 2$ eV and solve for the magnetic field using Eq. 12. We find the ion density by assuming the ion velocity at the exit plane to be $T_{\text{AF}_0}/\dot{m}$, so that

$$n_{\text{e}} = \frac{1000 \dot{m}^2 N_{\text{A}}}{\pi r_{\text{ae}}^2 M T_{\text{AF}_0}}, \tag{29}$$

where N_{A} is Avogadro's number.

We expect that as β_{ae} increases, the value of $\hat{r}_{\text{a-}\Phi}$ at which $\hat{s}$ is minimized, or $\hat{r}^*_{\text{a}}$, will correspondingly increase due to the gasdynamic pressure forcing the ions across field lines. We group the data in bins by β_{ae} value in Fig. 15 and see this is in fact the case. This dependence indicates that the effective area over which the Lorentz force acts is governed by a balance of the gasdynamic and magnetic pressures in thrusters for which the anode expands more rapidly than the magnetic field.

VIII. Conclusions

We find that each of the existing models incorrectly describes the thrust dependence on electrode and solenoid geometry. Our empirical fit to the data using nondimensional analysis shows that we can better predict the data by accounting for the degree to which the anode inner surface follows the magnetic field contour. Based on this improved agreement, we show that a substantial cause for disagreement between $JB_{\text{A}}r_{\text{a}}$ thrust models and measurement is a result of variability in the effective anode radius resulting from the magnetic pressure, which restricts the area over which the Lorentz force acts for certain magnetic field topologies.

Acknowledgments

This research was carried out with support from the Program in Plasma Science and Technology through the Princeton Plasma Physics Laboratory. We are grateful to Willow Dressel for her help locating many of the sources cited in this paper.

References

[1] G. Kruelle. Characteristics and local analysis of MPD thruster operation. In *AIAA Electric Propulsion and Plasmadynamics Conference*, AIAA-67-672, Colorado Springs, CO, Sept. 11–13, 1967. `doi:10.2514/6.1967-672`.

[2] D. Brown, B. Beal, and J. Haas. Air Force Research Laboratory high power electric propulsion technology development. Technical report, IEEEAC, 2009.

[3] E. Musk. Spacex interplanetary transport system. URL: `http://www.spacex.com/mars`.

[4] V. Tikhonov, S. Semenikhin, J. R. Brophy, and J. E. Polk. The experimental performances of the 100 kW Li MPD thruster with external magnetic field. In *24th International Electric Propulsion Conference*, IEPC-95-105, Moscow, Russia, Sept. 19–23, 1995.

[5] G. Herdrich, A. Boxberger, D. Petkow, R. A. Gabrielli, S. Fasoulas, M. Andrenucci, R. Albertoni, F. Paganucci, and P. Rosetti. Advanced scaling model for simplified thrust and power scaling of an applied-field magnetoplasmadynamic thruster. In *46th AIAA/ASME/SAE/ASEE Joint Propulsion Conference*, AIAA-2010-6531, Nashville, TN, July 25–28, 2010. `doi:10.2514/6.2010-6531`.

[6] L. K. Rudolph. *The MPD Thruster Onset Current Performance Limitation.* PhD thesis, Princeton University, Sept. 1980.

[7] А. Г. Попов and С. А. Семенихин. Расчет Тяги Торцевого Холловского Ускорителя (calculation of thrust for the end-Hall effect rocket). In *VII Всесоюзная Конференция по Плазменным Ускорителям и Ионным Инжекторам (7th Soviet Conference for Plasma Rockets and Ion Injectors)*, pp. 202-203, Kharkiv, Ukraine, Sept. 26–28, 1989.

[8] G. Popov, V. Kim, T. Tikhonov, S. Semenikhin, and M. Tibrina. The third quarterly report on the stages ## 5-6 of the contract on the research studies no. NASA-4851 between RIAME MAI and NASA. Technical Report NASW-4851, RIAME MAI, June 1995.

[9] R. Albertoni, F. Paganucci, and M. Andrenucci. A phemenological model for applied-field MPD thrusters. *Acta Astronautica*, 107:177–186, 2015. `doi:10.1016/j.actaastro.2014.11.017`.

[10] H. Maecker. Plasmaströmungen in lichtbögen infolge eigenmagnetischer kompression (plasma jets in arcs in a process of self-induced magnetic compression). *Zeitschrift für Physik*, 141(1):198–216, 1955.

[11] E. Y. Choueiri. Scaling of thrust in self-field magnetoplasmadynamic thrusters. *Journal of Propulsion and Power*, 14(5):744–753, 1998. `doi:10.2514/2.5337`.

[12] M. Coletti. A thrust formula for an MPD thruster with applied-magnetic field. *Acta Astronautica*, 81:667–674, 2012. `doi:10.1016/j.actaastro.2012.08.014`.

[13] A. Sasoh and Y. Arakawa. Thrust formula for applied-field magnetoplasmadynamic thrusters derived from energy conservation equation. *Journal of Propulsion and Power*, 11(2):351–356, 1995. `doi:10.2514/3.51432`.

[14] D. B. Fradkin, A. W. Blackstock, D. J. Roehling, T. F. Stratton, M. Williams, and K. W. Liewer. Experiments using a 25 kW hollow cathode lithium vapor MPD arcjet. In *AIAA 7th Electric Propulsion Conference*, AIAA-69-2417, Williamsburg, VA, Mar. 3–5, 1969. `doi:10.2514/6.1969-241`.

[15] R. M. Myers. Scaling of 100 kW class applied-field MPD thrusters. In *28th Joint Propulsion Conference and Exhibit*, AIAA-92-3462, Nashville, TN, July 6–8, 1992.

[16] P. G. Mikellides and P. J. Turchi. Applied-field magnetoplasmadynamic thrusters, part 2: Analytic expressions for thrust and voltage. *Journal of Propulsion and Power*, 16(5):894–901, 2000. `doi:10.2514/2.5657`.

[17] V. B. Tikhonov, S. A. Semenikhin, V. A. Alexandrov, and G. A. Popov. Research of plasma acceleration processes in self-field and applied magnetic field thrusters. In *23rd International Electric Propulsion Conference*, IEPC-93-076, Seattle, WA, Sept. 13–16, 1993.

[18] V. B. Tikhonov, S. A. Semenikhin, J. R. Brophy, and J. E. Polk. Performance of 130 kW MPD thruster with an external magnetic field and Li as a propellant. In *25th International Electric Propulsion Conference*, IEPC-97-117, Cleveland, OH, Aug. 24–28, 1997.

[19] V. Kim, T. Tikhonov, and S. Semenikhin. The second quarterly report on the stages ##2A, B of the contract on the research studies no. NASW-4851 between RIAME MAI and NASA. Technical Report NASW-4851, RIAME MAI, July 1996.

[20] V. Kim, T. Tikhonov, and S. Semenikhin. The fourth quarterly (final) report on the stage ## 3 “C”, “D” of the contract on the research studies no. NASW-4851 between RIAME MAI and NASA. Technical Report NASW-4851, RIAME MAI, Apr. 1997.

[21] R. M. Myers, M. Mantenieks, and J. Sovey. Geometric effects in applied-field MPD thrusters. In *21st International Electric Propulsion Conference*, AIAA-90-2669, Cleveland, OH, July 18–10, 1990.

[22] R. R. John and S. Bennett. Final report: Arcjet technology research and development. Technical Report NASA CR-54687/RAD-TR-65-37, AVCO Corporation, NASA Contract NAS 3-5900, Dec. 1965.

[23] S. Bennett, G. Enos, R. John, and W. Powers. Final report: Magnetoplasmadynamic thrustor research. Technical Report NASA CR-72345/AVSSD-0272-67-RR, AVCO Missiles, Space, and Electronics Group, NASA Contract NAS 3-8907, May 1967.

[24] R. M. Myers, A. J. Kelly, and R. G. Jahn. Energy deposition in low-power coaxial plasma thrusters. *Journal of Propulsion*, 7(5):732–739, 1991. `doi:10.2514/3.23386`.

[25] D. Lev. *Investigation of Efficiency in Applied Field MagnetoPlasmaDynamic Thrusters.* PhD thesis, Princeton University, Jan. 2012.

[26] G. Serianni, N. Vianello, F. Paganucci, and P. Rossetti. Plasma diagnostics in an applied field MPD thruster. In *27th International Electric Propulsion Conference*, IEPC-2001-135, Pasadena, CA, Oct. 15–19, 2001.

[27] A. V. Arefiev and B. N. Breizman. Magnetohydrodynamic scenario of plasma detachment in a magnetic nozzle. *Physics of Plasmas*, 12(043504), 2005. `doi:10.1063/1.1875632`.

[28] J. M. Little and E. Y. Choueiri. Divergence of a propulsive plasma flow expanding through a magnetic nozzle. In *31st International Electric Propulsion Conference*, IEPC-2009-260, Ann Arbor, MI, Sept. 20–24, 2009.

[29] E. Ahedo and M. Merino. On plasma detachment in propulsive magnetic nozzles. *Physics of Plasmas*, 18(053504), 2011. `doi:10.1063/1.3589268`.

[30] R. G. Jahn. *Physics of Electric Propulsion*, chapter 8, pages 240–244. Dover Publications, Inc., Mineola, NY, 1968.

[31] J. Gilland and G. Johnston. MPD thruster performance analytic models. In *Space Technology and Applications International Forum*, Albuquerque, NM, Feb. 2–5, 2003.

[32] V. Kim, T. Tikhonov, and S. Semenikhin. The second quarterly report on the stages ## 3-4 of the contract on the research studies no. NASA-4851 between RIAME MAI and NASA. Technical Report NASW-4851, RIAME MAI, Jan. 1995.

[33] P. J. Turchi. *The Cathode Region of a Quasi-Steady Magnetoplasmadynamic Arcjet.* PhD thesis, Princeton University, Sept. 1970.

[34] A. P. Bruckner and R. G. Jahn. Spectroscopic studies of the exhaust plume of a quasi-steady MPD accelerator. Technical Report 1041, NASA Research Grant NGL 31-001-005, 1972.

[35] H. Tobari, A. Ando, M. Inutake, and K. Hattori. Characteristics of electromagnetically accelerated plasma flow in an externally applied magnetic field. *Physics of Plasmas*, 14(093507), 2007. `doi:10.1063/1.2773701`.

[36] H. Tahara, H. Yasui, Y. Kagaya, and T. Yoshikawa. Development of a quasi-steady MPD arcjet thruster for near-earth missions. In *19th AIAA/DGLR/JSASS International Electric Propulsion Conference*, AIAA-87-1001, Colorado Springs, CO, Mar. 11–13, 1987. `doi:10.2514/6.1987-1001`.

[37] D. Ichihara, T. Uno, H. Kataoka, J. Jeong, A. Iwakawa, and A. Sasoh. Ten-ampere-level, applied-field-dominant operation in magnetoplasmadynamic thrusters. *Journal of Propulsion and Power*, 33(2):360–369, 2017. `doi:10.2514/1.B36179`.

[38] S. Yokota, D. Ichihara, H. Kataoka, S. Harada, and A. Sasoh. Steady-state, applied-field, rectangular MPD thrusters. In *33rd International Electric Propulsion Conference*, IEPC-2013-246, Washington, D.C., Oct. 6–10, 2013.

[39] F. Paganucci, P. Rossetti, M. Andrenucci, V. B. Tikhonov, and V. A. Obukhov. Performance of an applied field MPD thruster with a pre-ionization chamber. In *33rd Plasmadynamics and Lasers Conference*, AIAA-2002-2103, Maui, HI, May 20–23, 1964. `doi:10.2514/6.2002-2103`.

[40] N. Koyama, T. Suzuki, T. Kubota, and H. Tahara. Performance characteristics of steady-state MPD thrusters with permanent magnets and multi hollow cathodes for in-space propulsion. In *33rd International Electric Propulsion Conference*, IEPC-2013-094, Washington, D.C., Oct. 6–10, 2013.

[41] W. J. Coogan. AF-MPDT database. URL: `http://alfven.princeton.edu/tools/afmpdt-database`.

[42] J. S. Sovey and M. A. Mantenieks. Performance and lifetime assessment of magnetoplasmadynamic arc thruster technology. *Journal of Propulsion*, 7(1):71–83, 1991. `doi:10.2514/3.23296`.

[43] R. M. Myers. Applied-field MPD thruster geometry effects. Technical Report NASA CR-187163/AIAA-91-2342, Sverdum Technology, Inc., Lewis Research Center Group, NASA Contractor Report 187163, Aug. 1991.

[44] H. Kurtz. *Integrale Messungen an einem Axialsymmetrischen Elektronmagnetischen Plasmabeschleuniger (Triebwerksmodell X-13) (Integral Measurements on an Axial-symmetric Electromagnetic Plasma Thruster (Model X-13)).* PhD thesis, Deutsche Forschungs und Versuchsanstalt für Luft und Raumfahrt, Aug. 1971.

[45] R. E. Jones. Results of large vacuum facility tests of an MPD arc thruster. *AIAA Journal*, 4(8):1455–1456, 1966. `doi:10.2514/3.3705`.

[46] G. Krülle and E. Zeyfang. Preliminary conclusions of continuous applied field electromagnetic thruster research at DFVLR. In *AIAA 11th Electric Propulsion Conference*, AIAA-75-417, New Orleans, LA, Mar. 19–21, 1975. `doi:10.2514/6.1975-417`.

[47] G. L. Cann, R. A. Moore, R. L. Harder, and P. F. Jacobs. High specific impulse thermal arcjet thrustor technology part II: Performance of Hall arc jets with lithium propellant. Technical Report AFAPL-TR-65-48, Part II, Electro-Optical Systems, Inc., Jan. 1967.

[48] G. L. Cann, R. L. Harder, and R. A. Moore. Hall current accelerator. Technical Report NASA CR-54705/EOS 5470-Final, Electro-Optical Systems, Inc., Feb. 1966.

[49] A. D. Kodys and E. Y. Choueiri. A critical review of the state-of-the-art in the performance of applied-field magnetoplasmadynamic thrusters. In *41st AIAA/ASME/SAE/ASEE Joint Propulsion Conference and Exhibit*, AIAA-2005-4247, Tucson, AZ, July 11–13, 2005. `doi:10.2514/6.2005-4247`.

[50] G. Krülle, M. Auweter-Kurtz, and A. Sasoh. Technology and application aspects of applied field magnetoplasmadynamic propulsion. *Journal of Propulsion*, 14(5):754–763, 1998. `doi:10.2514/2.5338`.

[51] D. R. Lev and E. Y. Choueiri. Scaling of efficiency with applied magnetic field in magnetoplasmadynamic thrusters. *Journal of Propulsion and Power*, 28(3):609–616, 2012. `doi:10.2514/1.B34194`.

[52] Н. В. Белан, В. П. Ким, А. Е. Оранский, and В. Б. Тихонов. *Стационарные Плазменные Двигатели (Stationary Plasma Engines)*, chapter 5, pages 128–131. Kharkiv Aviation Institute, Kharkiv, Ukraine, 1989.

[53] G. I. Barenblatt. *Scaling, Self-Similarity and Intermediate Asymptotics*, chapter 1, pages 28–63. Cambridge University Press, New York, NY, 1996.

[54] J. D. Huba. *NRL Plasma Formulary*, page 28. Naval Research Laboratory, Washington, D.C., 2016.

[55] R. Albertoni, P. Rossetti, F. Paganucci, M. Andrenucci, M. Zuin, E. Martinez, and R. Cavazzana. Experimental study of a 100-kW class applied-field MPD thruster. In *32nd International Electric Propulsion Conference*, IEPC-2011-110, Wiesbaden, Germany, Sept. 11–15, 2011.

[56] R. Albertoni, F. Paganucci, P. Rossetti, and M. Andrenucci. Experimental study of a hundred-kilowatt-class applied-field magnetoplasmadynamic thruster. *Journal of Propulsion and Power*, 29(5):1138–1145, 2013. `doi:10.2514/1.B34688`.

[57] R. Albertoni. Personal Correspondence, Oct. 9, 2016.

[58] D. B. Fradkin and D. J. Roehling. Thrust stand performance measurements of a lithium fueled applied field MPD arcjet. In *13th Symposium on the Engineering Aspects of Magnetohydrodynamics*, Stanford, CA, Mar. 26–28, 1973.

[59] D. B. Fradkin and D. J. Roehling. Experiments in the new LASL MPD arcjet test facility. Technical Report LA-5199-MS, Los Alamos, Feb. 1973.

[60] R. A. Moore, G. L. Cann, and L. R. Gallagher. High specific impulse thermal arcjet thrustor technology part I: Performance of Hall arc jets with lithium propellant. Technical Report AFAPL-TR-65-48, Part I, Electro-Optical Systems, Inc., June 1965.

[61] G. L. Cann, R. A. Moore, P. F. Jacobs, and L. R. Gallagher. High specific impulse thermal arcjet thrustor technology. Technical Report AFAPL-TR-65, Electro-Optical Systems, Inc., Sept. 1965.

[62] W. Grossman Jr., R. V. Hess, and H. A. Hassan. Experiments with a coaxial Hall current plasma accelerator. *AIAA Journal*, 3(6):1034–1039, 1965. `doi:10.2514/3.3050`.

[63] W. Grossman Jr., R. V. Hess, and H. A. Hassan. Experiments with a co-axial Hall current plasma accelerator. In *AIAA 4th Electric Propulsion Conference*, AIAA-64-700, Philadelphia, PA, Aug. 31–Sept. 2, 1964. `doi:10.2514/6.1964-700`.

[64] M. A. Mantenieks, J. S. Sovey, R. M. Myers, T. W. Haag, P. Raitano, and J. E. Parkes. Performance of a 100 kW class applied field MPD thruster. In *25th Joint Propulsion Conference*, AIAA-89-2710, Monterey, CA, July 10–12, 1989. `doi:10.2514/6.1989-2710`.

[65] T. W. Haag. Design of a thrust stand for high power electric propulsion devices. In *25th Joint Propulsion Conference*, AIAA-89-2829, Monterey, CA, July 10–12, 1989. `doi:10.2514/6.1989-2829`.

[66] R. M. Myers. Electromagnetic effects in an applied-field magnetoplasmadynamic thruster. *Journal of Propulsion and Power*, 11(2):343–350, 1995. `doi:10.2514/3.51431`.

[67] R. M. Myers. Applied-field MPD thruster performance with hydrogen and argon propellants. *Journal of Propulsion and Power*, 9(5):781–784, 1993. `doi:10.2514/3.23691`.

[68] P. G. Mikellides, P. J. Turchi, and N. F. Roderick. Applied-field magnetoplasmadynamic thrusters, part 1: Numerical simulations using the MACH2 code. *Journal of Propulsion and Power*, 16(5):887–893, 2000. `doi:10.2514/2.5656`.

[69] V. Kim, T. Tikhonov, and S. Semenikhin. The first quarterly report on the stage ## 3 A of the contract on the research studies no. NASW-4851 between RIAME MAI and NASA. Technical Report NASW-4851, RIAME MAI, Apr. 1996.

[70] G. Popov, V. Kim, T. Tikhonov, S. Semenikhin, and M. Tibrina. The fourth (final) quarterly report on the milestones (a) (4) and (a) (5) (D) of SoW of contract no. 960938 between RIAME MAI and JPL. Technical Report 960938, RIAME MAI, Dec. 1998.

[71] V. B. Tikhonov, S. A. Semenikhin, and J. E. Polk. Own magnetic field impact on MPD thrusters performance with external magnetic field. In *26th International Electric Propulsion Conference*, IEPC-99-176, Kitakyushu, Japan, Oct. 17–21, 1999.

[72] H. Tahara, Y. Kagaya, and T. Yoshikawa. Hybrid MPD thruster with axial and cusp magnetic fields. In *20th International Electric Propulsion Conference*, IEPC-1988-058, Garmisch-Partenkirchen, West Germany, Oct. 3–6, 1988.

[73] H. Tahara, Y. Kagaya, and T. Yoshikawa. Performance and acceleration process of quasisteady magnetoplasmadynamic arcjets with applied magnetic fields. *Journal of Propulsion and Power*, 13(5):651–658, 1997. `doi:10.2514/2.5216`.

[74] H. Tahara, F. Takiguchi, Y. Kagaya, and T. Yoshikawa. Performance characteristics and discharge features of a quasi-steady applied-field MPD arcjet. In *22nd International Electric Propulsion Conference*, IEPC-1991-073, Viareggio, Italy, Oct. 14–17, 1991.

[75] H. Tahara, Y. Kagaya, and T. Yoshikawa. Effects of applied magnetic fields on performance of a quasisteady magnetoplasmadynamic arcjet. *Journal of Propulsion and Power*, 11(2):337–342, 1995. `doi:10.2514/3.51430`.

[76] D. Ichihara. Personal Correspondence, Jan. 6, 2017.

[77] A. Sasoh and Y. Arakawa. Electromagnetic effects in an applied-field magnetoplasmadynamic thruster. *Journal of Propulsion and Power*, 8(1):98–102, 1992. `doi:10.2514/3.23448`.

[78] A. Sasoh, A. E. Solem, and Y. Arakawa. Optimization of current distribution in an applied-field MPD thruster. In *20th International Electric Propulsion Conference*, IEPC-1988-057, Garmisch-Partenkirchen, West Germany, Oct. 3–6, 1988.

[79] T. Nakano, A. Ishiyama, Y. Shimizu, and K. Toki. Feasibility study of a low-power applied-field MPD arcjet. In *28th International Electric Propulsion Conference*, IEPC-2003-092, Toulouse, France, Mar. 17–21, 2003.

[80] R. E. Jones and E. L. Walker. Status of large vacuum facility tests of MPD arc thrustor. In *3rd Aerospace Sciences Meeting*, AIAA-66-117, New York, NY, Jan. 24–26, 1966. `doi:10.2514/6.1966-117`.

[81] D. W. Esker, J. C. Kroutil, and R. J. Checkley. Radiation cooled MPD arc thruster. Technical Report NASA CR-72557/MDC-H296, McDonnell Research Laboratories, NASA Contract NAS 3-11518, July 1969.

A. Sasoh and Arakawa Model Parameter Estimation

The Sasoh and Arakawa model depends on a number of variables that are not defined in terms of controllable parameters. The Hall parameter, for instance, depends on the collision frequency between electrons and ions, ν_{ei}. We use the relation[54]

$$\nu_{\mathrm{ei}} = 3.64 \times 10^{-6} n_{\mathrm{e}} \frac{\log\left(1.24 \times 10^{7} \sqrt{\mathcal{T}_{\mathrm{e}}^{3}/n_{\mathrm{e}}}\right)}{\mathcal{T}_{\mathrm{e}}^{1.5}} \tag{30}$$

to determine this parameter, where $\mathcal{T}_{\mathrm{e}}$ is electron temperature in K and n_{e} is electron density in m^{-3}. Because electron temperatures from 1–10 eV have been reported for AF-MPDTs,[8, 24–26] we solve for the thrust using this full range of temperatures, giving a range of possible thrust values.

We model n_{e} using the continuity equation and assume that $n_{\mathrm{i}} = n_{\mathrm{e}}$. $\dot{m}$ and the area of the anode exit plane are known, but we require the ion velocity through this plane, u_{ex}. The ion velocity exiting the anode volume is $T/\dot{m}$, but because we need this density estimation in order to determine T, we use the full range of possible exit velocities found in the database, 0.8–86 km/s. Our final expression is

$$n_{\mathrm{e}} = \frac{1000 \dot{m} N_{\mathrm{A}}}{\pi r_{\mathrm{ae}}^{2} M u_{\mathrm{ex}}}, \tag{31}$$

where N_{A} is Avogadro's number and M is the ion mass. The range of possible exhaust velocity values results in a range of calculated thrust values.

The Sasoh and Arakawa model requires a characteristic length scale which they denote as r^{*}. It is unclear how this value is determined, but in the example they provide in Ref. 13, the given value is approximately $1/10^{\mathrm{th}}$ the distance from the cathode radius to the anode radius, and so we use the expression

$$r^{*} = r_{\mathrm{c}} + \frac{r_{\mathrm{a}} - r_{\mathrm{c}}}{10}. \tag{32}$$

In order to solve for the radial and axial components of the magnetic field, we use the Biot Savart law for a solenoid. This can be difficult to evaluate off the thrust axis, but if we model the strength of the magnetic field strictly as a function of axial distance from the solenoid, z, we can choose an area, $A(z)$ enclosing a magnetic flux Φ. Setting Φ as a constant, we can evaluate the area $A(z + dz)$ at some small distance dz downstream enclosing that same flux. After solving for the change in area, we determine trigonometrically which components of the magnetic field are axial and which are radial at the edge of the surface of interest. In this case, we choose the area at the exit plane of the anode and evaluate the magnetic field strength using Eq. 12.

B. Propellant Properties

Table 5: Propellant properties used in analysis.

	H_2	He	Li	N_2	NH_3	Na	Ar	K	Kr	Xe	Cs
M (u)	2.02	4.00	6.94	28.01	17.03	22.99	39.95	39.10	83.80	131.29	132.91
ϵ_{i} (eV)	15.42	24.59	5.39	15.58	10.20	5.14	15.76	4.34	14.00	12.13	3.89
γ	1.41	1.67	1.67	1.41	1.28	1.67	1.67	1.67	1.67	1.67	1.67

C. Catalogued Thrusters

Table 6: Catalogued thrusters and their operating regimes.

Thruster	Principal Investigators	Power (kW)	B_A (T)	Propellants	p_b (mTorr)	Error Reported?	Electrode Geometry	Refs.
Alta	Albertoni et al.	21–230	0–0.1	Ar	0.15	Y	conical, dir.	9, 55–57
H2-1	Cann et al.	38–89	0.1–0.3	H_2	150	N	conical, del.	48
H2-2 (D – F)	Cann et al.	4–14	0.2–0.7	H_2	20–40	N	cylindrical	48
H2-3B	Cann et al.	8–17	0.3	H_2	50	N	cylindrical	48
H2-4 (A – E)	Cann et al.	7–13	0.3	H_2	15–30	N	conical, del.	48
H2-4F	Cann et al.	4–13	0.3	H_2, He, N_2, Ar	0.05–70	N	conical, del.	48
HC-8	Fradkin and Roehling	14	0.2	Li	0.02	Y	cylindrical	58, 59
LAJ-AF (2 – 4)	Moore et al.	7–23	0.3–0.5	Li	0.7–1000	Y	cylindrical	60
LAJ-AF-6D	Cann et al.	3–34	0.2–0.5	Li, Na, K	0.5	Y/N	cylindrical	47, 48, 61
LAJ-BF-1D	Cann et al.	4–16	0.08–0.2	K	0.1	Y	cylindrical	47
LAJ-CF (3 – 5)	Moore et al.	6–38	0.5	Li	30–1000	Y	cylindrical	60
LaRC	Grossmann et al.	8–36	0.1–0.6	Ar	5	N	cylindrical	62, 63
LeRC-A0	Mantenieks, Myers, et al.	20–48	0–0.3	Ar	0.5	Y	conical, del.	21, 64, 65
LeRC-B0	Mantenieks, Myers, et al.	30–45	0.02–0.2	Ar	0.5	Y	conical, dir.	21, 64, 65
LeRC-C0	Myers et al.	29–72	0.02–0.04	Ar	0.5	Y	cylindrical	21, 65
LeRC-A	Myers	15–87	0.03–0.2	H_2, Ar	0.5	Y	cylindrical	15, 43, 66, 67
LeRC (B, C, E – G)	Myers	24–120	0.03–0.2	Ar	0.5	Y	cylindrical	15, 43, 66, 68
LeRC-H	Myers	38–59	0.03–0.1	Ar	0.5	Y	conical, dir.	43, 66
MAI-30kW	Kim et al.	12–38	0.06–0.1	Li	5	Y	conical, dir.	69
MAI-130kW	Tikhonov et al.	53–120	0.05–0.09	Li	4	Y	conical, dir.	4, 18–20
MAI-200kW	Tikhonov et al.	120–180	0.05–0.3	Li	5	Y	conical, dir.	70, 71
MY-I	Tahara et al.	230–4,900	0–0.3	H_2, NH_3	0.008	Y	cylindrical	72
MY-III	Tahara et al.	98–4,900	0–0.5	H_2, NH_3, Ar	0.008	Y	conical, del.	36, 72–75
MY-III (C1-1, C1-3, C1-3-CA.L, C1-3-CO.L, C2-12, C2-23, C3-123)	Tahara et al.	360–3,900	0.05–0.5	H_2, NH_3	0.008	Y	conical, del.	36, 72

Thruster	Principal Investigators	Power (kW)	B_A (T)	Propellants	p_b (mTorr)	Error Reported?	Electrode Geometry	Refs.
NaU-A	Ichihara et al.	0.7–3	0.1–0.3	Ar	0.4	Y	conical, dir.	37, 76
ToU	Sasoh et al.	2–10	0.03–0.3	H_2, N_2, Ar	1	Y	conical, del.	77, 78
WaU (s, m, l)	Nakano et al.	0.4–1	0.1–0.2	Ar	0.5	Y	conical, del.	79
X-2C	John and Bennett	18–170	0.08–0.3	H_2, NH_3	100	Y	conical, dir.	22, 80
X-2C-H2O	John and Bennett	5–12	0.07–0.3	Cs	0.1	Y	conical, dir.	22
X-2C-Rad	John and Bennett	4–7	0.01–0.3	Li	0.1	Y	conical, dir.	22
X-7 (s, m, l, xl)	Esker et al.	13–38	0.1–0.2	NH_3	10	N	conical, del.	81
X-7 (C-1 – C-5, CR)	Bennett et al.	9–100	0.08–0.3	NH_3	100	N	conical, del.	23
X9	Krülle	22–96	0-0.3	H_2, Ar	500	N	conical, del.	1
X13	Kurtz	5–89	0.1–0.4	Ar	10	N	cylindrical	44
X16	Krülle and Zeyfang	3–12	0.6	Ar, Kr, Xe	0.6	N	conical, del.	46